Intensified and apace bauxitization over the paleo-karstic surface linked to volcanism

Xuefei Liu[1], Qingfei Wang[1,†], Yongbo Peng[2,†], Runsheng Yin[3], Yao Ma[1], Lihua Zhao[1], and Shangqing Zhang[4]

[1]*State Key Laboratory of Geological Processes and Mineral Resources, China University of Geosciences, Beijing 100083, China*
[2]*International Center for Isotope Effect Research, Nanjing University, Nanjing 210023, China*
[3]*State Key Laboratory of Ore Deposit Geochemistry, Institute of Geochemistry, Chinese Academy of Sciences, Guiyang 550002, China*
[4]*College of Geoscience and Survey Engineering, China University of Mining and Technology (Beijing), Beijing 100083, China*

ABSTRACT

Recent studies indicate that volcanism may be a potentially important factor in the formation of karstic bauxite, but more evidence is needed. Six billion tons of bauxite formed upon paleo-karstic terrain within a short time in the Late Carboniferous in the North China Basin (NCB) and in the Late Permian in the Youjiang Basin (YB) of China. The factors that trigger their apace formation remain unclear. Herein, we proposed that extensive volcanic eruptions have accounted for this large-scale bauxite formation based on the mineralogy, Hg isotopes, and Hg concentration enrichment proxies of the samples of bauxitic sequence in the NCB and YB. NCB bauxite generally has three layers, namely bottom Fe-bearing claystone, intermediate bauxite ore, and top claystone, while bottom Fe-bearing claystone is usually absent in YB bauxite, which directly covers carbonate rocks. The mineral assemblages of NCB and YB bauxite confirm that they were deposited in a superficial alkaline and reducing karstic environment. Strong Hg enrichment peaks with corresponding near-zero Δ^{199}Hg, a signal of excess volcanogenic Hg, were discovered in the upper claystone of NCB bauxitic sequences, which overlaid the Ordovician carbonate substrate. It denotes volcanism occurred immediately subsequent to deposition of terrestrial weathered Al-rich remnants in paleo-karstic depressions during the Late Carboniferous. This volcanism, occurring in the northern margin of the NCB, is considered to have triggered the apace bauxitization in the NCB after its long exposure and weathering. In the YB, the remarkable Hg enrichment and near-zero Δ^{199}Hg were observed in the entire Late Permian bauxitic sequences with Late Permian carbonate as the substrate. It denotes enhanced volcanogenic Hg inputs throughout the whole deposition process of bauxite during the Late Permian. This episode of volcanism associated with the Emeishan large igneous province and contemporaneous arc system resulted in the short term weathering of source materials and the apace bauxitization in YB. Volcanism is suggested to aggravate surface acidic and oxidizing conditions, in which rapid decomposition of source materials occurred to release Al^{3+} to precipitate diaspore above the physiochemical barrier of underlying carbonate.

1. INTRODUCTION

The formation of karstic bauxite was previously considered to be jointly controlled by the palaeoclimatology, tectonic instability, eustatic fluctuations, and palaeogeography of continents and oceans (Bárdossy, 1982; Bárdossy and Combes, 1999). Recent research on karstic bauxite around the world by mineralogy, geochemistry, and detrital zircon dating also indicate contributions from igneous rocks (volcanic rocks were assured in some cases) to the karstic bauxite (Fig. 1A; Deng et al., 2010; Wang et al., 2016; Yu et al., 2016; Hou et al., 2017; Kelemen et al., 2017; Radusinović et al., 2017; Abedini et al., 2021; Mongelli et al., 2014, 2021). This recent advance makes us consider whether volcanism was an important but long-ignored factor controlling the formation of karstic bauxite. Evidence is required to assure the participation of massive volcanic materials in karstic deposition formation.

Six billion tons of diaspore-dominant karstic bauxites were formed upon paleo-karstic terrain within the Late Permian to Late Carboniferous in the North China Basin (NCB) and Youjiang Basin (YB) of China (Fig. 1B; Liu et al., 2020; Wang et al., 2020). Geological and mineralogical studies have shown that the formation mechanism of these bauxites is distinct from those in the Urals, Mediterranean, and Iran-Himalaya, where the diaspores were considered to form through prolonged burial and metamorphic processes (Fig. 1A; Bogatyrev et al., 2009). The occurrences of mineral assemblages indicated the diaspores were deposited in a superficial karstic environment and in volcanic rocks related to oceanic subduction and mantle plume which suggest these environments contributed materials to the karstic bauxite in the NCB and YB (Deng et al., 2010; Wang et al., 2016).

According to the age variation of the youngest detrital zircons in the bauxite layer and the sedimentary age of the overlying and underlying strata of the bauxite determined by fossils, it was revealed that the bauxite was formed within a transient period, i.e., ∼5 billion tons of bauxite in the whole NCB formed within 20 Ma, and one billion tons of bauxite in YB formed within 10 Ma (Wang et al., 2016; Hou et al., 2017; Liu et al., 2017). Factors leading to the intensified and apace bauxitization still remain poorly understood. We suspected that extensive volcanism might trigger bauxite formation in the NCB and YB, as it could lead to climatic warming and accelerated chemical weathering (Grasby et al., 2017; Shen et al., 2022), however, evidence for this hypothesis is lacking. More comparative research on the sedimentary sequences and mineral compositions between NCB and YB was required to find their similarities and differences in sedimentary settings and surface Ph-Eh conditions. In addition, analysis of Hg content and isotopic compositions can aid in revealing large volcanisms in geological history (Selin, 2009; Sanei et al., 2012; Thibodeau et al., 2016; Grasby et al., 2017; Shen et al., 2019a). Large volcanism can lead to transit emission of massive amounts

Qingfei Wang https://orcid.org/0000-0002-2883-6921
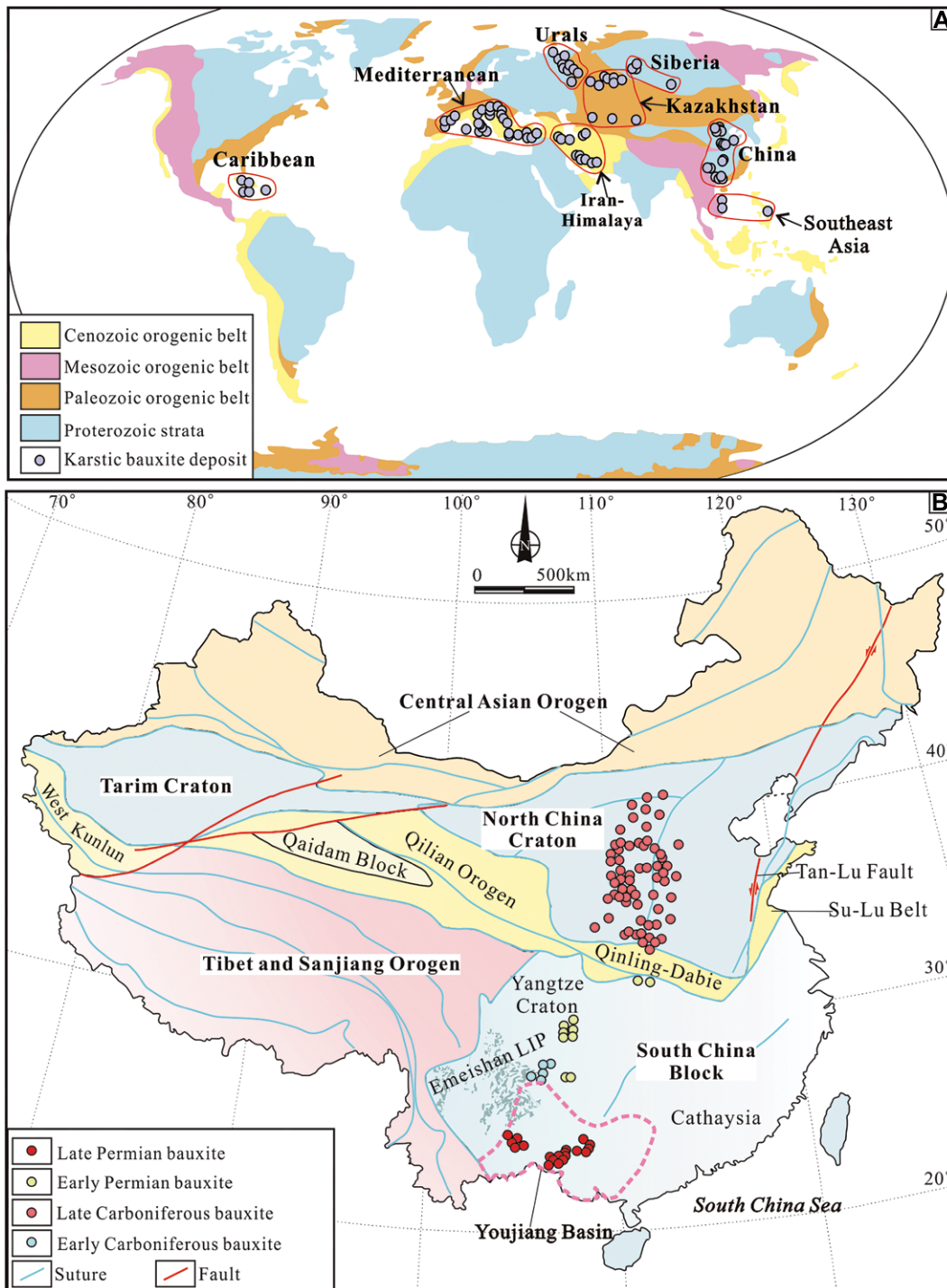†Corresponding authors: wqf@cugb.edu.cn; ybpeng@nju.edu.cn.

1187

Figure 1. (A) World map showing distribution of karstic bauxite deposits, modified after Bogatyrev et al. (2009) and Mondillo et al. (2021). (B) Geological map showing the distribution of bauxite deposits in China, modified after Deng et al. (2010), Liu et al. (2017, 2020), and Wang et al. (2020). LIP—large igneous province.

of Hg to the environment and cause anomalous high Hg concentrations and remarkable Hg isotopic shifts in sediments (Grasby et al., 2019; Shen et al., 2019b).

Here, two representative bauxite deposits, the Xinxian bauxite deposit from the NCB and the Gaoji bauxite deposit from YB, were chosen for investigation. Both deposits have great resource reserves of bauxite (e.g., 0.3 billion tons in Xinx-

ian and 0.2 billion tons in Gaoji). Geological and mineralogical features, mercury concentrations, and isotopic compositions of bauxite-bearing strata (e.g., underlying limestone, Fe-bearing claystone, bauxite ore, and claystone), were analyzed from drill cores from the two deposits, to understand the link between extensive volcanism and the intensified and apace bauxite formation over the paleo-karstic surface.
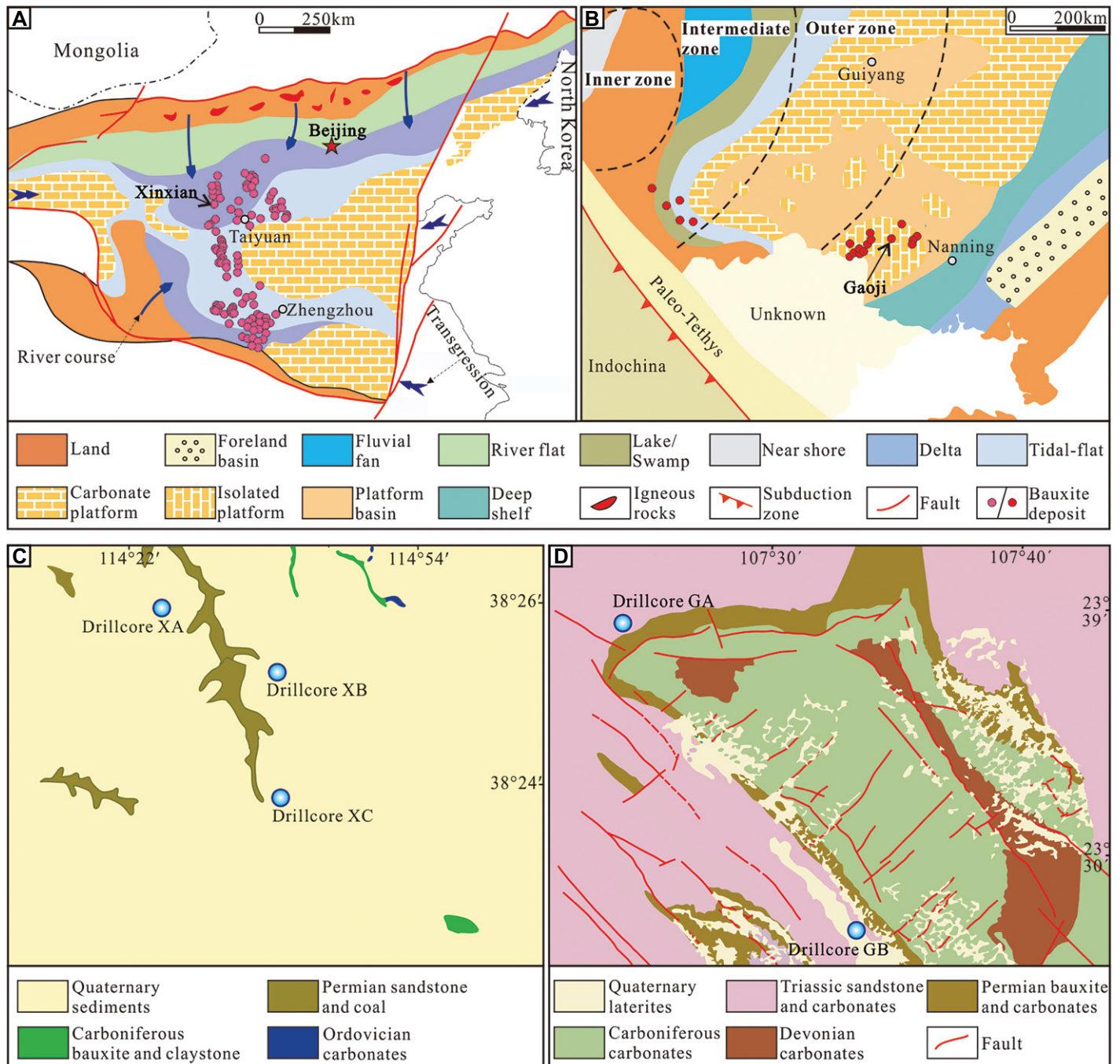
2. TECTONIC EVOLUTION

2.1. Tectonic Evolution of the NCB during Paleozoic Exposure (445–300 Ma)

From the Middle Ordovician to Late Carboniferous (445–300 Ma), the North China Block drifted from the equator to 30° N (Veevers, 2004). The low latitudes enabled the NCB

to undergo intense chemical weathering (Wang et al., 2018). In most areas of the NCB, Middle Ordovician limestone (the Majiagou Formation) was exposed and experienced karstification, forming widespread karstic topography (Liu, 2011). Large-scale weathered iron ore (known as the "Shaanxi-type" iron ore) and ferric claystone in karstic high-ground and ferrous claystone in

karstic depressions were formed from the underlying carbonates during this period (Liu et al., 2013; Zhao and Liu, 2019). From ca. 320 to 300 Ma, large-scale bauxite ore and claystone were deposited upon the Fe-bearing claystone and weathered iron ore (Fig. 2A; Zhao and Liu, 2019), throughout the NCB with varying thicknesses (Liu et al., 2013). The source rocks of

the bauxite ore and claystone are allochthonous and are dominated by 450 and 950 Ma igneous rocks and Precambrian metamorphic rocks in the southern NCB, and by 320–300 Ma igneous rocks and Precambrian metamorphic rocks in the northern NCB (Wang et al., 2016, 2018; Zhao and Liu, 2019). During the Late Carboniferous, the NCB evolved as a walled continental

Figure 2. (A) Late Carboniferous paleogeographic map of the North China Basin, modified after Wang et al. (2018). (B) Late Permian paleogeographic map of the Youjiang Basin of China and its neighboring region, modified after Wang et al. (2020), inner, intermediate, and outer zones here refer to the zoning of Emeishan large igneous province. (C) Geological map of Xinxian bauxite deposit showing drill core positions. (D) Geological map of Gaoji bauxite deposit showing drill core positions.

basin because the Paleozoic Bainaimiao and North Qinling arc systems were accreted to the north and south of NCB, respectively (Fig. 2A; Wang et al., 2016). Igneous zircons with ages of 320–300 Ma have been found in bauxite ore and claystone throughout the NCB (Zhao and Liu, 2019). Based on the widespread development of Late Carboniferous magmatism along the northern margin of the NCB (Fig. 2A; Zhang et al., 2007, 2009; Deng et al., 2018), large volcanism has been proposed to explain the existence of these igneous zircons (Liu et al., 2014; Wang et al., 2018). Late Carboniferous plutons, consisting mainly of quartz diorites, diorites, granodiorites, tonalites, and some hornblende gabbros, are subduction-related rocks that were emplaced at an Andean-style continental margin. The formation of these plutons was a result of anatectic melting of the underplated ancient lower crust, with variable involvement of enriched mantle materials during the southward subduction of the Paleo-Asian oceanic plate beneath the NCB (Wang et al., 2016).

2.2. Tectonic Evolution of the Youjiang Basin during the Permian–Triassic Transition

The YB was formed during the Devonian as a result of rifting of Cambrian–Ordovician units within the South China Block (SCB) (Du et al., 2009; Wang et al., 2020), and it was located near the equator from the Late Permian to Early Triassic (Veevers, 2004). Permian to Early Triassic sediments within the YB are dominated by carbonate and marine clastic and pyroclastic rocks (Mei et al., 2007; Liu et al., 2017; Wang et al., 2020). Isolated Permian–Triassic carbonate platforms were widely developed within the basin (Fig. 2B; Mei et al., 2007). The western Guangxi platform, one of the isolated carbonate platforms, was exposed at the end of the Middle Permian induced by the Emeishan plume upwelling (Fig. 2B; He et al., 2010). Transient exposure of the carbonate rocks led to the formation of Fe-bearing claystone and weathered iron ore overlying the Maokou limestone. Subsequent Emeishan volcanic eruption provided sufficient source materials and suitable conditions for large-scale bauxite formation within a period of 10 Ma (Liu et al., 2017; Wang et al., 2020). The basin was then filled by clastic detritus in the Middle–Upper Triassic as a result of the closure of the Paleo-Tethyan branch ocean (Cai and Zhang, 2009). During this period (ca. 260 Ma), the nearby Emeishan large igneous province (LIP) was active. The Emeishan LIP covers an area of more than 2.5×10^5 km², with a total thickness ranging from several hundred meters up to 5 km (Xu et al., 2001; Deng et al., 2010).

Three zones (inner, intermediate, and outer) were spatially divided in terms of the Emeishan LIP, and the western Guangxi platform is within the outer zone (Fig. 2B; Xu et al., 2001). The Emeishan LIP is mainly composed of voluminous mafic volcanic successions, numerous contemporaneous mafic intrusions, and some felsic rocks including syenites, a felsic magmatic rock (Chung and Jahn, 1995; Zhou et al., 2002; Shellnutt and Zhou, 2007). In addition, the Paleo-Pacific Ocean was subducted along the southern margin of the YB (Deng and Wang, 2016; Li et al., 2018; Wang et al., 2020) and the Ailaoshan-Song Ma Paleo-Tethyan Ocean crust subducted westwards during this period (Fig. 2B; Deng et al., 2014, 2021b). Volcanism induced by the subduction of the Paleo-Pacific was also believed to have contributed to the formation of YB bauxite (Wang et al., 2020).

3. GEOLOGY OF BAUXITE DEPOSITS

3.1. Carboniferous Bauxite Deposits in the NCB

Although bauxite and claystone were deposited in most areas of the NCB during the Late Carboniferous, bauxite deposits with industrial value are mainly found in Shanxi and Henan provinces (Figs. 1B and 2A). More than 100 bauxite deposits and occurrences have been discovered in these two provinces (Fig. 2A). The reserves of bauxite are well over 5 billion tons, surpassing Jamaica's reserves and making this the largest karstic bauxite belt in the world (Bogatyrev et al., 2009; Liu, 2011). Carboniferous bauxite and claystone overlap Ordovician carbonate karstic terrain and are hosted in the lower member of the Benxi Formation (Fig. 3). The bauxite and claystone are further overlain by sandstone and/or carbonates of the upper member of the Benxi Formation (Fig. 3; Wang et al., 2016). The lower layer in the paleo-karst uplift area is commonly dominated by ferric mineral-bearing claystone and/or weathered iron ore (Figs. 3A and 3D; Liu et al., 2020), whereas in depressions formed by the paleo-karstic topography, the principal components are ferrous and clay minerals (Fig. 3A). The middle layer consists of oolitic and massive bauxite ores of varying thicknesses, whose distributions are mainly controlled by the paleo-karstic topography (Fig. 3; Liu, 2011). Thick bauxite ores mainly occur in the paleo-karstic depressions (Fig. 3B). In paleo-karst uplift areas, the ores are relatively thin or even absent (Figs. 3A and 3D; Liu et al., 2020). The upper layer is claystone, which generally has a gradual transitional contact with the underlying bauxite ore (Figs. 3B and 3C). The bauxite ores commonly have a less oxidized,

pale-colored matrix, occasionally accompanied by pale ooids and/or intraclasts (Figs. 3B–3D). The Xinxian bauxite deposit is located in the central part of the Carboniferous bauxite concentration area in the NCB (Fig. 2A). Within the bauxite deposit, most areas are covered by Quaternary sediments with only minor outcrops of Ordovician limestone, Carboniferous bauxite ore and claystone, and Permian coal and sandstone (Fig. 2C).

3.2. Permian Bauxite Deposits in Youjiang Basin

Permian bauxite deposits in the YB were mainly developed in the western Guangxi area (Fig. 2B). More than one billion tons of bauxite ore have been discovered (Liu et al., 2010; Zhang, 2011). The bauxite ore, belonging to the lower member of the Late Permian Heshan Formation, was deposited in the karstic depressions of paleo-karstic topography developed on Permian Maokou carbonates (Fig. 4). It was then overlain by carbonate of the upper member of the Heshan Formation (Fig. 4; Liu et al., 2017). In contrast to the Carboniferous bauxite in the NCB, in most cases, bauxite ore in YB directly covers the Maokou carbonate paleo-karstic surface without an intervening Fe-bearing claystone layer (Fig. 4A and D; Liu et al., 2017). A thin weathered crust layer only occurs in areas of uplifted karst topography (Fig. 4B; Yang et al., 2021). Above the bauxite ore, a claystone layer is widely developed and shows a gradual transitional contact relationship with the underlying bauxite ore (Fig. 4C; Liu et al., 2017). The bauxite ores are generally characterized by cryptocrystalline and oolitic textures, enrichment in pyrite and organic matter, and are dark in color (Figs. 4A–4C). The Gaoji bauxite deposit is in the central part of the western Guangxi bauxite concentration area (Fig. 2B). It mainly comprises Devonian to Permian carbonates, Permian bauxite and claystone, Early Triassic sandstone and carbonate, and Quaternary laterite (Fig. 2D). NW and NE trending faults are widely developed (Fig. 2D).

4. SAMPLING AND ANALYTICAL METHODS

4.1. Sample Collection

Three drill cores from the lower member of the Benxi Formation in the Xinxian bauxite deposit located in the central NCB (Figs. 2A and 2C), and two drill cores from the lower member of the Heshan Formation in the Gaoji bauxite deposit located in central YB (Figs. 2B and 2D), were selected for mineralogical compositions,
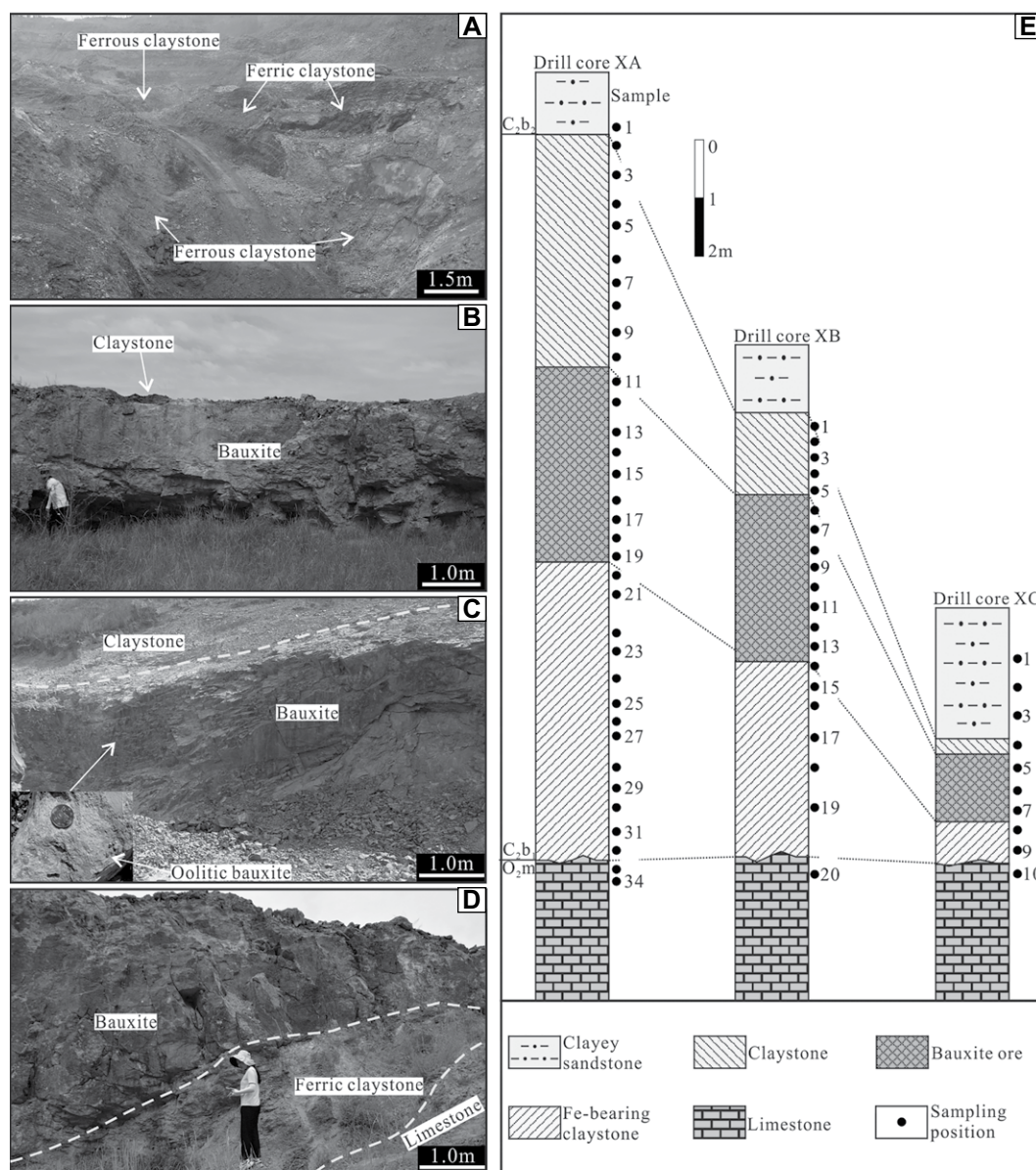
Figure 3. Field photos and drill core profiles from the Xinxian bauxite deposit of China showing the sequence composition of the ore-bearing rock series: (A) an open pit showing the mineral compositions of the Fe-bearing claystone in different paleo-karst topography: the karstic depression being dominated by ferrous and clay minerals, whereas ferric and clay minerals in the karstic uplifted area; (B) massive bauxite ore being gradually transforming upward into claystone; (C) oolitic bauxite ore being changing into claystone upward; (D) limestone, ferric clay, and bauxite ore from bottom to top in a paleo-karst uplift; and (E) profiles from three drill cores in the Xinxian bauxite deposit showing the sample collection locations.

Hg concentrations and isotopic composition, total sulfur (TS), total organic carbon (TOC), and carbon isotopic composition analyses. 34, 20, and 10 samples were taken from drill cores XA, XB, and XC, respectively, in the Xinxian bauxite deposit (Fig. 3E), while 19 and 28 samples were gathered from drill cores GA and GB, respectively, in the Gaoji bauxite deposit (Fig. 4D).

4.2. Mineralogical Analyses

Mineral compositions and associated parageneses of all samples were obtained using X-ray diffraction (XRD), electron probe microanalysis (EPMA), and scanning electronic microscopy (SEM) analyses at the China University of Geosciences (Beijing, China). XRD analyses were conducted using a Rigaku D/Max-RC diffractometer (Rigaku Corp., Japan) with a CuKá1 radiation source. EPMA was performed using a Shimadzu EPMA-1720 instrument, using an accelerating voltage of 15 kV, a beam current of 10 nA, an acquisition time of 50 s, and a beam diameter of 1 μm. SEM was undertaken using a HITACHI S-450 instrument at a pressure of 1 bar, an ambient temperature of 21 ± 0.5 °C, and a humidity of $46 \pm 1\%$.

The mineral concentrations of all analyzed samples were estimated using the relative intensity ratio (RIR) method, and corundum (a-Al_2O_3) was chosen as the standard for comparing the diffraction intensities of the powdered materials (Bishop et al., 2011; Zanoni et al., 2016). The principles of this method have been described in detail by Zhou et al. (2018). The RIR value is calculated based on the following equation (Hillier, 2000):

$$RIR_{i,s} = \left(\frac{X_s}{X_i} \right) * \left(\frac{I_{(hkl)i}}{I_{(hkl)_s}} \right) * \left(\frac{I^{rel}_{(jkl)_s}}{I^{rel}_{(hkl)i}} \right). \quad (1)$$

where X is the weight fraction of the tested samples, I is the intensity of the characteristic reflection, I^{rel} is the relative intensity of the reflection, and i and s are the clay mineral sample and internal standard phase, respectively. Herein, corundum was chosen as an internal standard. To obtain the RIR_{cor} value, a binary system composed of corundum and a clay mineral
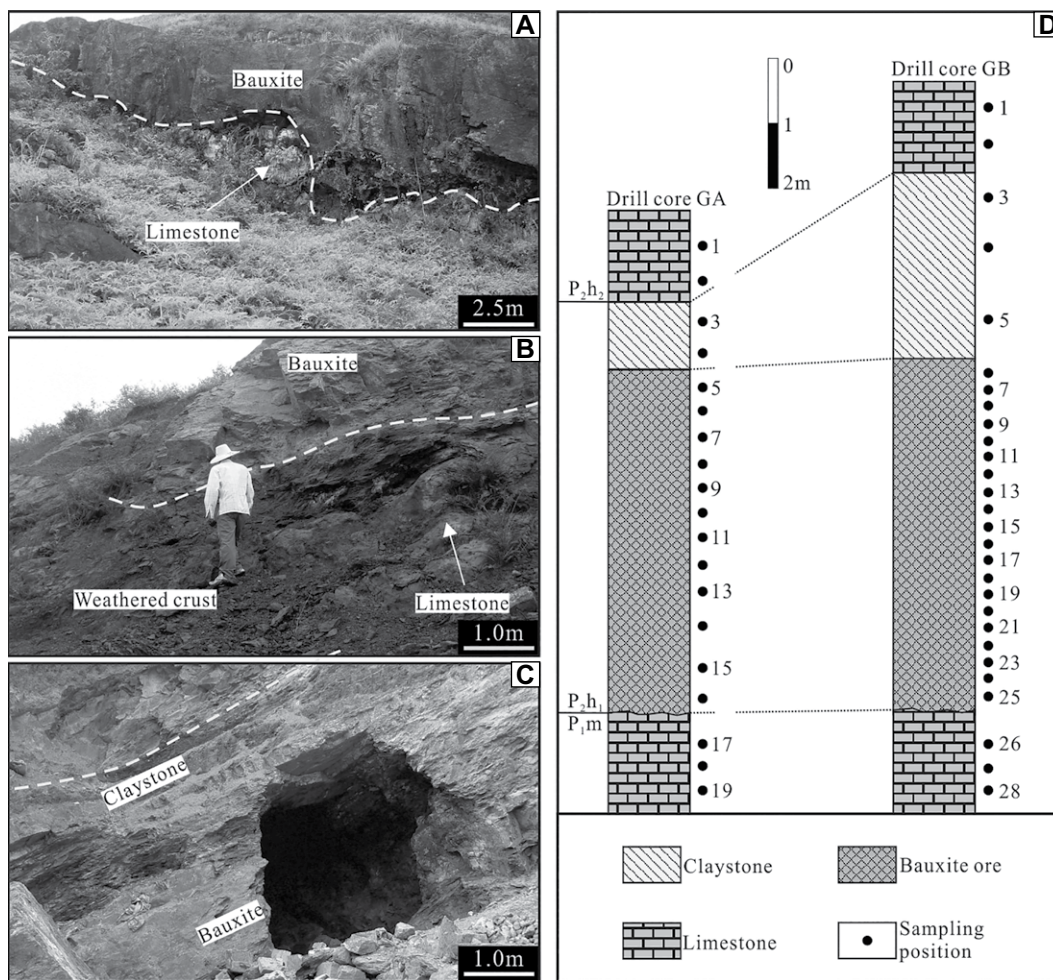
Figure 4. Field photos and drill core profiles from the Gaoji bauxite deposit of China showing the sequence composition of the ore-bearing rock series: (A) bauxite ore directly overlying on the underlying Maokou limestone; (B) weathered crust being composed of ferric minerals and clay minerals developing in local paleo-karst uplift area; (C) massive bauxite ore gradually changing into claystone upward; and (D) profiles from two drill cores in the Gaoji bauxite deposit showing the sample collection locations.

was prepared, with a 1:1 mass ratio of corundum and clay mineral. The RIR_{cor} value was then determined based on the intensities of the most intense corundum reflection ($I_{(113)cor}$) and clay mineral reflection ($I_{(hkl)i}$) (Hillier, 2000). After calculating RIR_{cor}, the concentration of any phase i in a sample spiked with a known amount of corundum is given by Hillier (2000) as follows:

$$X_i = \left(\frac{X_{cor}}{RIR_{cor}}\right) * \left(\frac{I_{(hkl)i}}{I_{(113)cor}}\right). \quad (2)$$

4.3. Mercury Concentrations and Isotopic Analyses

All samples were pulverized to 200 mesh in an agate mortar. A total of 52 bauxite ore samples, 21 Fe-bearing claystone samples, 20 upper claystone samples, 4 clayey sandstone samples, and 10 limestone samples were chosen for Hg concentration and isotopic composition analyses (Figs. 3E and 4D), at the Institute of Geochemistry, Chinese Academy of Sciences.

Approximately 0.2 g of each sample was digested (95 °C, 6 h) in 2 mL of aqua regia (HCl/HNO$_3$ = 3/1, v/v). Hg concentration was measured using cold-vapor atomic absorption spectrometry (F732S, Shanghai Huaguang Instrument Corp.), which has a detection limit of 0.05 ng/mL. A standard reference material (GSS-4, soil) was prepared and measured every 10 samples, which yielded Hg recoveries of 90%–100%. The solutions were dissolved to 0.5 ng/mL Hg in 10% HCl (v/v). The 18.2 MΩ•cm water was used for the preparation of all reagents and solutions. Hg isotope analysis was conducted using a Neptune Plus multi-collector–inductively coupled plasma–mass spectrometer (Yin et al., 2016). Mercury concentrations and acid matrices in the bracketing NIST SRM 3133 solutions were matched with 10% of the neighboring samples. Mercury isotopic compositions are reported following the convention proposed by Bergquist and Blum (2007). Specifically, mass-dependent fractionation is expressed in δ^{202}Hg notation in units of ‰ referenced to the NIST-3133 Hg standard (analyzed before and after each sample):

$$\delta^{202}Hg(\text{‰}) = \left[\frac{(^{202}Hg/^{198}Hg_{sample})/}{(^{202}Hg/^{198}Hg_{standard})-1}\right] \times 1000. \quad (3)$$

Mass-independent fractionation is reported in Δ notation, which describes the difference between the measured δ^{xxx}Hg and the theoretically predicted δ^{xxx}Hg value, in units of ‰:

$$\Delta^{xxx}Hg \approx \delta^{xxx}Hg - \delta^{202}Hg \times \beta. \quad (4)$$

β is equal to 0.2520 for ^{199}Hg, 0.5024 for ^{200}Hg, and 0.7520 for ^{201}Hg. Analytical uncertainty was estimated based on the replication of the NIST-3177 secondary standard solution and GSS-4 digested solution. The overall average and uncertainty of NIST-3177 (δ^{202}Hg: −0.50 ± 0.11‰; Δ^{199}Hg: −0.02 ± 0.06‰; Δ^{201}Hg: −0.03 ± 0.07‰; 2SD, n = 14) and GSS-4 (δ^{202}Hg: −1.71 ± 0.12‰; Δ^{199}Hg: −0.37 ± 0.07‰; Δ^{201}Hg: −0.39 ± 0.06‰; 2SD, n = 6) agree well with comparable previous studies (Bergquist and Blum, 2007; Deng et al.,

2021a). The larger values of standard deviation (2SD) for either NIST-3177 or GSS-4 reflect the analytical uncertainties.

4.4. Total Sulfur, Total Organic Carbon, and Carbon Isotope Analyses

All samples analyzed for Hg concentrations and isotope compositions were also analyzed for TS, TOC, and carbon isotopes. TS, TOC, and $\delta^{13}C_{org}$ were measured using a Vario microcube elemental analyzer coupled with an Isoprime 100 mass spectrometer in the oxyanion stable isotope consortium at Louisiana State University. An aliquot of 1–3 g of bulk-sample powder was decarbonated overnight in a polypropylene centrifuge tube with 3% (v/v) HCl. The process was repeated at least three times to ensure complete carbonate removal. The carbonate-free residues were then neutralized using Milli-Q water following a stepwise washing procedure, and dried at 70 °C. Samples (~50 mg) were loaded into capsules and flash-combusted at 1060 °C in a Vario microcube elemental analyzer. The resulting CO_2 gas was measured by a thermal conductivity detector to obtain the TOC (wt%) and then transferred by continuous flow for isotopic ratio determination on an Isoprime 100 mass spectrometer. The conventional delta notation is used to report $^{13}C/^{12}C$ ratio as a per million deviations from the Vienna Pee Dee belemnite standard. Calibration of the $d^{13}C$ values was accomplished using an acetanilide working standard ($d^{13}C = -27.6‰$). Sample $d^{13}C$ values were repeatable to a standard error of 0.1‰. Furthermore, ~50 mg of each sample was loaded into capsules and flash-combusted at 1000 °C in a Vario microcube elemental analyzer. The resulting SO_2 gas was measured by a thermal conductivity detector to obtain the TS (wt%).

5. RESULTS

5.1. Mineral Compositions and their Occurrences

5.1.1. Xinxian Bauxite Deposit in the NCB

The three drill cores from the Xinxian bauxite deposit have the same mineral compositions in equivalent horizons (e.g., bauxite ore) (Table S1[1];

---

[1]Supplemental Material. Table S1: Mineral concentrations of samples from three drill cores in Xinxian bauxite deposit by the relative intensity ratio method based on X-ray diffraction results. Table S2: Mineral concentrations of samples from two drill cores in Gaoji bauxite deposit by the relative intensity ratio method based on X-ray diffraction results. Please visit https://doi.org/10.1130/GSAB .S.20318466 to access the supplemental material, and contact editing@geosociety.org with any questions.

Fig. 5A). The Fe-bearing claystone is dominated by chlorite, berthierine, illite, and amorphous materials. The bauxite ore contains diaspore, anatase, illite, berthierine, chlorite, kaolinite, and pyrite (Figs. 5A and 6). The upper claystone mainly consists of kaolinite, illite, diaspore, and anatase. All three drill cores of this study have high contents of clay minerals, especially the bottom Fe-bearing claystone layer and the upper claystone layer, in which the clay concentrations are greater than 50% (Table S1). Backscattered SEM and SEM images of the bauxite ore show that diaspore is closely associated with pyrite, anatase, chamosite, and berthierine in Xinxian (Figs. 6A–6F). Diaspore intimately coexists with framboidal pyrite that is widespread in the bauxite ore (Fig. 6A). It also occurs as fine particles within anatase or pyrite aggregates (Figs. 6B and 6C). Diaspore with high crystallinity is occasionally found, which coexists closely with anatase (Fig. 6D). Ooids consisting of diaspore and chamosite are widespread and aggregates composed of diaspore and berthierine are also widely developed in the ore (Figs. 6E and 6F). Kaolinite mainly occurs in the form of aggregate, in which sporadic diaspore particles are developed (Fig. 6G). Dissolution fissures and pits are observed in the kaolinite aggregate (Fig. 6G). Microorganisms are preserved within the bauxite ore (Fig. 6H).

5.1.2. Gaoji Bauxite Deposit in the YB

The two drill cores from the Gaoji bauxite deposit mostly have similar mineral compositions in equivalent horizons (e.g., bauxite ore) except for the extra presence of some quartz and illite in drill core GB (Table S2 [see footnote 1]; Fig. 5B). The bauxite ore is composed of diaspore, pyrite, anatase, kaolinite, pyrophyllite, quartz, illite, and minor parisite, calcite, xenotime, and zircon, while the upper claystone consists of kaolinite, pyrophyllite, illite, diaspore, chlorite, pyrite, anatase, zeophyllite, quartz, calcite, and gypsum (Table S2; Figs. 5B and 7A–7H). SEM images of the bauxite ore show that diaspore is closely associated with pyrite, anatase, parisite, and organic matter (Figs. 7A–7E). Diaspore intimately coexists with framboidal pyrite (Fig. 7A), and also occurs within pyrite aggregates as minor inclusions (Fig. 7B). Meanwhile, fine pyrite grains are found to be cemented by diaspore as well (Fig. 7C). Mineral assemblage consisting of diaspore and anatase is widely found in ores (Fig. 7D). Abundant parisites have been identified under the SEM observation and it closely coexists with diaspore, pyrite, pyrophyllite, and organic matter (Figs. 7E and 7F). In the bauxite ore, kaolinite usually exists as veined aggregates interspersed with aggregates of diaspore and pyrite formed at an earlier stage (Fig. 7G); It also

commonly occurs in the peripheral or internal cracks of diaspore aggregate, and has a gradual transition relationship with diaspore (Fig. 7H). Organic matter is widespread in the bauxite ore (Figs. 7A, 7E, and 7F).

5.2. Mercury Concentrations and Isotopes and their Variations

5.2.1. Xinxian Bauxite Deposit in the NCB

In drill core XA, samples showed an average background Hg value of 183 ppb (Table 1; Fig. 8). A Hg-enriched horizon was observed in the lower part of the upper claystone layer (412–897 ppb). Negative $\Delta^{199}Hg$ values (–0.35‰ to –0.03‰) were observed throughout this profile, but a positive shift of 0.10‰ in $\Delta^{199}Hg$ was observed within the Hg-enriched horizon (Fig. 8). The $\delta^{202}Hg$ values ranged from –1.26‰ to 0.65‰, and a slight negative shift of –0.59‰ in $\delta^{202}Hg$ was observed in the Hg-enriched horizon (Fig. 8). The $\delta^{13}C_{org}$ values in this drill core ranged from –25.42‰ to –16.04‰. A negative shift of $\delta^{13}C_{org}$ (–16.04‰ to –22.38‰) was also observed in the lower part of the bauxite ore layer (Fig. 8). Samples of the bauxite ore, Fe-bearing claystone, and claystone overall had extremely low TOC and TS levels of <0.1% (Table 1; Fig. 8), while they all contained high total clay mineral (TCM) contents, except for a few samples in the bauxite ore (less than 10%) (Fig. 8).

In drill core XB, samples showed an average background Hg value of 168 ppb (Table 1; Fig. 8). However, the bottom of the upper claystone layer showed Hg concentrations of 515–647 ppb (Fig. 8). The $\Delta^{199}Hg$ values in this drill core ranged from –0.34‰ to –0.09‰, with the Hg-enriched horizon containing fewer negative values (–0.15‰ to –0.13‰; Fig. 8). The $\delta^{202}Hg$ values varied from –1.83‰ to –0.22‰, and a negative shift of $\delta^{202}Hg$ values occurred near the Hg-enriched horizon (Fig. 8). The $\delta^{13}C_{org}$ values ranged between –25.96‰ and –19.24‰, and a negative shift was also observed in the lower part of the bauxite ore layer (Fig. 8). TOC and TS concentrations in the bauxite ore, Fe-bearing claystone, and claystone of this drill core were also very low and mostly less than 0.1%, and the TCM was still very high in concentration except for a few samples from the bauxite ore (Table 1).

In drill core XC, samples showed an average Hg value of 215 ppb, with a Hg peak of up to 779 ppb occurring in the upper claystone layer (Table 1; Fig. 8). The $\Delta^{199}Hg$ values ranged from –0.28‰ to 0.00‰, with the less negative values located near the Hg-enriched horizon (0.00‰). The $\delta^{202}Hg$ values varied from –1.52‰ to –0.54‰, and higher $\delta^{202}Hg$ values were also found near the Hg-enriched horizon. The $\delta^{13}C_{org}$ values ranged from –25.80‰ to –19.64‰, with

Figure 5. Representative X-ray diffraction patterns of bauxite samples in drill core profiles of Xinxian bauxite deposit (A) and Gaoji bauxite deposit (B) of China. A—anatase; B—berthierine; C—chlorite; Ca—calcite; Ch—chamosite; D—diaspore; Di—dickite; Do—dolomite; Go—goethite; H—hematite; I—illite; K—kaolinite; Mu—muscovite; P—pyrophyllite; Py—pyrite; R—rutile; Q—quartz.

the lower part of the bauxite ore layer showing more negative values (Fig. 8). Extremely low contents of TOC and TS were also found in the Fe-bearing claystone, bauxite ore, and claystone (Table 1; Fig. 8). Both the upper claystone and underlying Fe-bearing claystone contained high levels of TCM, ranging from 38% to 97%, while the bauxite ore had relatively low contents of TCM, varying from 3% to 5% (Table 1).

5.2.2. Gaoji Bauxite Deposit in the YB

In drill core GA, the bauxite ore and claystone had very high Hg values (642–2170 ppb) compared with the underlying (49–56 ppb) and overlying (57 ppb) limestone (Table 2; Fig. 9). The Δ^{199}Hg values of all samples from the bauxite ore and claystone were close to zero (–0.10‰ to 0.07‰), and those from the underlying (–0.12‰ to –0.03‰) and overlying (0.22‰)

limestone showed small negative and positive shifts, respectively (Fig. 9). The δ^{202}Hg values ranged from –2.70‰ to –0.78‰ in the bauxite ore and claystone, and showed marked negative shifts compared with the underlying (–0.04‰ to 0.07‰) and overlying (0.73‰) limestone (Fig. 9). The $\delta^{13}C_{org}$ values in the bauxite ore and claystone were between –24.50‰ and –23.69‰ and were slightly heavier than the underlying
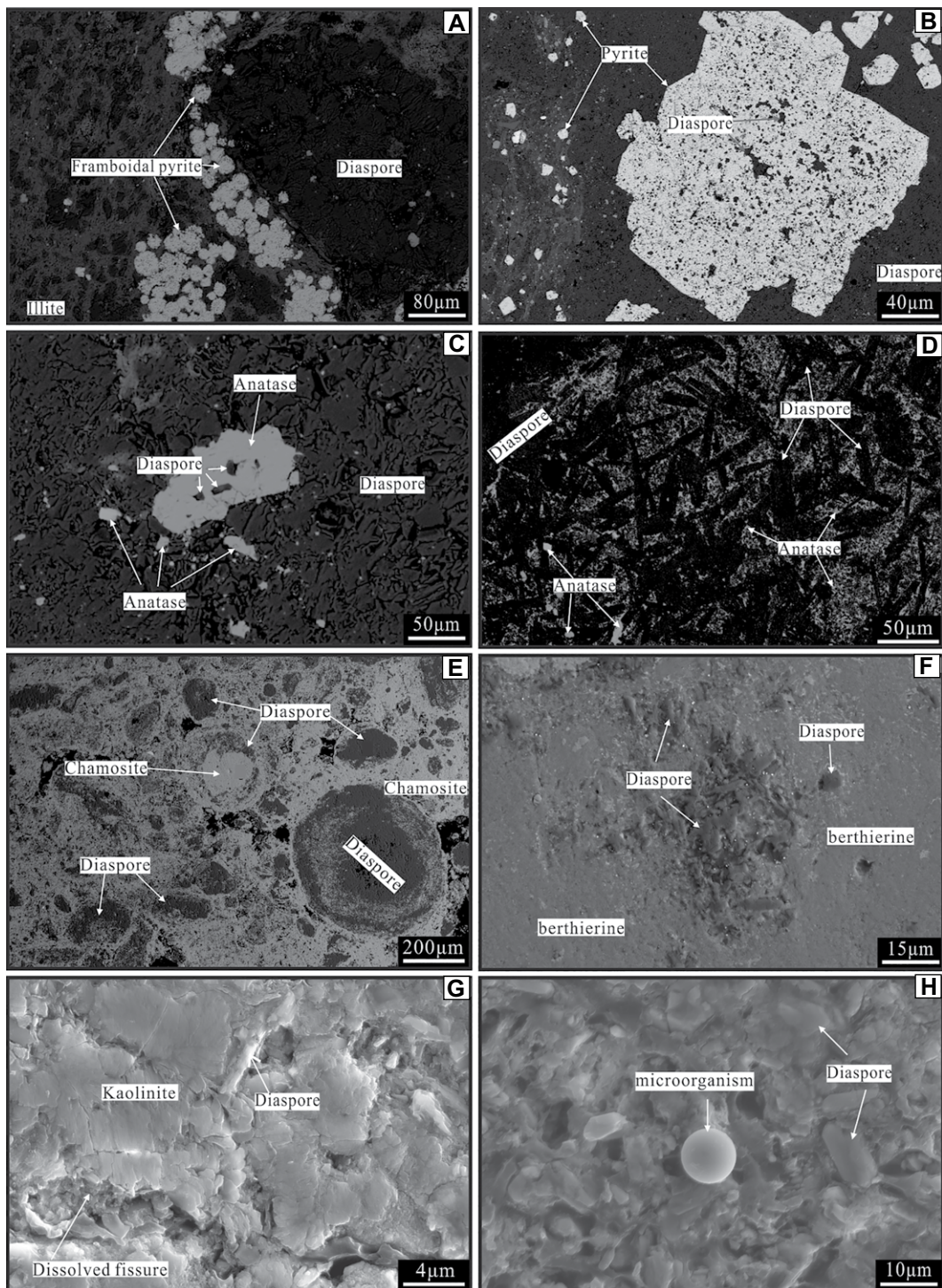
Figure 6. Backscattered scanning electronic microscopy (SEM) (A–D) and SEM (E–H) images from the Xinxian bauxite deposit of China showing the occurrence of major minerals: (A) coexistence of diaspore and framboidal pyrite in the bauxite ore with minor diaspore inclusions within the framboidal pyrite aggregate; (B) abundant fine diaspore inclusions within a pyrite particle; (C) diaspore and anatase coexisting with each other in the bauxite ore; (D) crystalline diaspore particles and anatase in the bauxite ore; (E) ooids formed by diaspore and chamosite located within the chamosite-dominant matrix; (F) coexistence of diaspore and berthierine in the bottom of the bauxite ore; (G) kaolinite aggregates with small amount of diaspore particle in the bauxite ore; and (H) preservation of microorganism in the bauxite ore.

(–26.05‰) and overlying (–25.10‰) limestone (Table 2). TOC concentrations in the bauxite ore and claystone ranged from 0.44% to 13.98%, and were mostly between 0.44% and 2.45%. The bauxite ore and claystone had high concentrations of TS with values ranging from 2.81% to 18.92%, while TS values in the underlying and overlying limestone were 13.74% and 0.28%, respectively (Table 2). High concentrations of

TCM were also observed in the bauxite ore and claystone (Table 2).

In drill core GB, compared with the underlying (4–76 ppb) and overlying (2–95 ppb) limestone, Hg was markedly enriched in the bauxite ore and claystone and showed a considerable variation in concentration from 86 to 1737 ppb (Table 2; Fig. 9). The Δ^{199}Hg values of the bauxite ore and claystone were between –0.04‰ and

0.11‰, with most close to zero (Fig. 9), which showed an evident negative shift compared with the underlying limestone (0.07‰ to –0.15‰), and little change compared with the overlying limestone (–0.05‰ to –0.01‰) (Fig. 9). The δ^{202}Hg values were –1.04‰ to –0.67‰, –1.16‰ to –0.40‰, and –1.33‰ to –0.55‰ in the underlying limestone, bauxite ore and claystone, and overlying limestone, respectively, and little
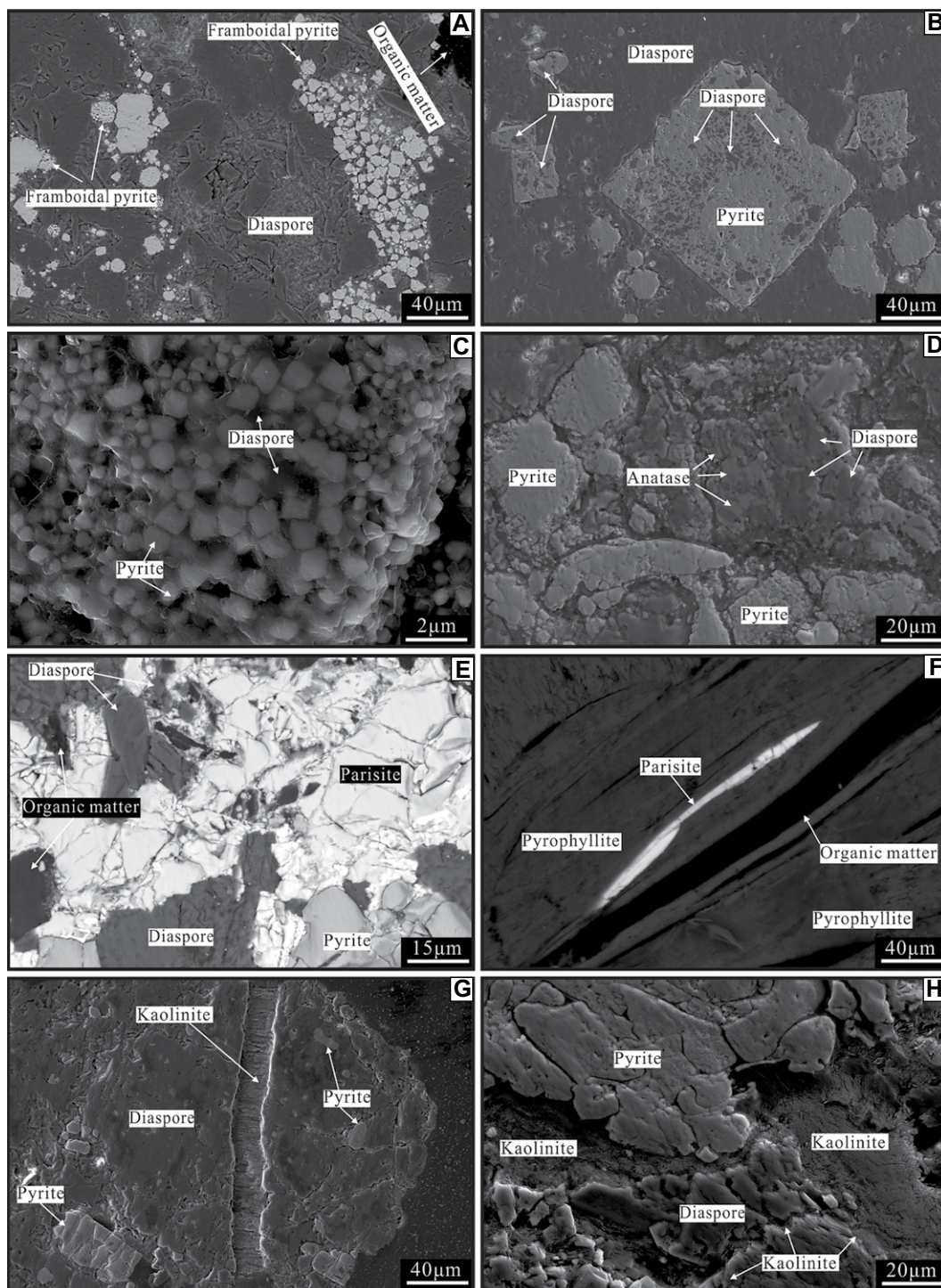
Figure 7. Scanning electronic microscopy images from the Gaoji bauxite deposit of China showing the occurrence of major minerals: (A) wide developments of framboidal pyrite and organic matter within the bauxite ore; (B) diaspore and pyrite coexisting with each other in the bauxite ore and wide development of diaspore inclusions in the pyrite grain; (C) fine pyrite particle being cemented by diaspore in the bauxite ore; (D) diaspore-anatase aggregate coexisting with pyrite in the bauxite ore; (E) extensive development of parisite in the bauxite ore and its close association with diaspore, pyrite, and organic matter; (F) intimate symbiosis between parisite and pyrophyllite in the ore; (G) kaolinite vein crossing the diaspore-pyrite assemblage; and (H) kaolinite developed along the periphery or internal fissures of diaspore aggregate.

variation was observed among them (Table 2). The $\delta^{13}C_{org}$ values in the bauxite ore and claystone were between –23.83‰ and –22.80‰, displaying a small positive shift compared with the underlying limestone (–24.18‰), and no clear change compared with the overlying limestone (–23.19‰ to –22.83‰) (Fig. 9). The bauxite ore and claystone were enriched in TOC (0.42% to 4.25%) compared with both the underlying (0.05% to 0.23%) and overlying (0.07% to 0.26%) limestone. Almost all samples from this drill core had high contents of TS, with those in the bauxite ore and claystone varying from 3.05% to 20.31% (Table 2). TCM content in this drill core was markedly enriched in the claystone layer (up to 94.3%), while in the bauxite ore it was between 1.8% and 12.1% (Table 2).

6. DISCUSSION

6.1. Depositional Conditions of Bauxite over the Paleo-Karstic Surface

The mineralogy of karstic bauxite faithfully records the redox conditions of the depositional environment (Valeton, 1972; D'Argenio and Mindszenty, 1995; Zarasvandi et al., 2012).

TABLE 1. ANALYZED SAMPLES FROM THE THREE DRILL CORES OBTAINED FROM THE XINXIAN BAUXITE DEPOSIT OF NORTH CHINA BASIN

Sample	Hg (ppb)	δHg^{202} (‰)	ΔHg^{199} (‰)	TOC (%)	δ^{13}C-VPDB (‰)	TS (%)	TCM (%)	Hg/TOC (ppb/%)	Hg/TS (ppb/%)	Hg/TCM (ppb/%)
XA-1	88	−0.74	−0.24	0.10	−24.09	0.14	97	861	623	1
XA-2	206	−0.72	−0.17	0.09	−24.77	0.08	94	2295	2711	2
XA-3	221	−0.75	−0.21	0.05	−25.42	0.02	98	4315	11729	2
XA-4	88			0.06	−24.58	0.01	97	1362	7474	1
XA-5	132	−0.68	−0.15	0.07	−22.28	0.01	98	2008	14142	1
XA-6	676	−0.75	−0.03	0.06	−24.01	0.01	95	10998	64914	7
XA-7	853	−1.10	−0.14	0.08	−24.04	0.01	95	10372	93613	9
XA-8	412	−0.93	−0.18	0.09	−22.96	0.01	94	4441	34672	4
XA-9	485	−1.26	−0.09	0.10	−23.78	0.01	97	4757	77325	5
XA-10	897	−0.88	−0.09	0.11	−23.30	0.01	98	8079	71878	9
XA-11	162	0.09	−0.28	0.07	−22.56	0.02	6	2202	10129	27
XA-12	176	0.12	−0.19	0.07	−22.18	0.02	3	2462	7582	59
XA-13	118	−0.64	−0.20	0.07	−22.53	0.02	50	1662	6787	2
XA-14	103	−0.31	−0.21	0.07	−22.20	0.02	30	1478	5157	3
XA-15	132	−0.85	−0.24	0.07	−20.73	0.04	49	1835	3586	3
XA-16	294	−1.15	−0.19	0.15	−21.00	0.04	56	1983	7261	5
XA-17	118	−0.29	−0.08	0.08	−22.25	0.03	80	1426	4677	1
XA-18	265	−0.84	−0.35	0.12	−22.38	0.04	71	2138	6906	4
XA-19	118	−0.16	−0.18	0.11	−16.04	0.02	90	1105	5215	1
XA-20	235	−0.42	−0.14	0.10	−16.89	0.02	88	2382	13956	3
XA-21	206	0.15	−0.35	0.11	−18.32	0.01	89	1920	14634	2
XA-22	397	−0.75	−0.20	0.13	−21.19	0.02	94	3162	22960	4
XA-23	162	−0.41	−0.19	0.05	−24.15	0.01	79	3233	14806	2
XA-24	191			0.05	−22.65	0.01	82	3496	14639	2
XA-25	74	0.65	−0.30	0.04	−21.95	0.02	84	1960	3863	1
XA-26	118	0.13	−0.30	0.05	−23.06	0.02	80	2504	6178	1
XA-27	132	0.16	−0.17	0.05	−23.38	0.02	62	2621	8534	2
XA-28	176	−0.44	−0.30	0.05	−19.95	0.02	92	3452	11025	2
XA-29	265	−0.34	−0.10	0.05	−22.66	0.01	96	5508	18919	3
XA-30	118	−0.64	−0.10	0.04	−23.96	0.01	72	2996	9504	2
XA-31	191	0.15	−0.24	0.05	−24.31	0.01	69	3874	24298	3
XA-32	368	−0.74	−0.16	0.06	−23.60	0.01	91	6545	44406	4
XA-33	279	−0.65	−0.16	0.10	−20.64	0.03	43	2697	10791	6
XA-34	176	−0.51	−0.20	0.17	−23.57	0.10	41	1044	1751	4
XB-1	176	−1.14	−0.26	0.03	−24.62	0.01	97	5738	21978	2
XB-2	132			0.05	−24.01	0.01	96	2822	14822	1
XB-3	118			0.04	−25.29	0.01	97	2829	12494	1
XB-4	515	−1.07	−0.15	0.12	−22.87	0.02	94	4267	23917	5
XB-5	647	−1.49	−0.13	0.04	−22.85	0.02	72	14782	34514	9
XB-6	221	−1.70	−0.09	0.06	−22.99	0.01	41	3441	18700	5
XB-7	206	−1.83	−0.09	0.07	−22.87	0.01	52	3165	16838	4
XB-8	147	−0.22	−0.19	0.06	−21.38	0.02	5	2380	7986	29
XB-9	191	−1.01	−0.21	0.09	−20.70	0.02	12	2221	11375	16
XB-10	176	−0.99	−0.34	0.10	−20.98	0.01	24	1708	15165	7
XB-11	147	−1.04	−0.15	0.10	−21.17	0.02	12	1473	7867	12
XB-12	162			0.09	−21.71	0.02	7	1903	7593	23
XB-13	88	−0.83	−0.24	0.10	−19.24	0.02	51	878	4347	2
XB-14	176			0.10	−20.43	0.02	13	1756	7914	14
XB-15	74	−0.75	−0.19	0.26	−23.04	0.03	100	286	2222	1
XB-16	176	−0.98	−0.18	0.10	−20.34	0.02	100	1748	10205	2
XB-17	147	−0.50	−0.14	0.09	−19.65	0.03	67	1599	4954	2
XB-18	132	−0.67	−0.22	0.05	−21.04	0.01	84	2597	16860	2
XB-19	265	−0.64	−0.15	0.04	−24.66	0.01	89	7166	25605	3
XB-20	294	−0.83	−0.25	0.08	−22.18	0.15	63	3712	1907	5
XC-1	147	−0.44	−0.20	0.09	−25.80	0.39	47	1594	375	3
XC-2	74	−0.71	−0.04	0.07	−24.26	0.23	38	1106	320	2
XC-3	235	−1.43	−0.04	0.08	−24.90	0.06	62	2818	3695	4
XC-4	779	−1.52	0.00	0.00	−24.74	0.03	67	1006081	28964	12
XC-5	118	−0.54	−0.09	0.06	−22.60	0.02	3	1967	5211	39
XC-6	265	−0.91	−0.09	0.06	−21.64	0.02	4	4540	11690	66
XC-7	279	−0.93	−0.20	0.06	−20.17	0.06	5	4619	4539	56
XC-8	265	−1.19	−0.17	0.10	−20.45	0.02	97	2671	15521	3
XC-9	250	−0.99	−0.28	0.10	−20.96	0.02	90	2542	10103	3
XC-10	309	−0.69	−0.18	0.16	−19.64	0.14	43	1887	2207	7

Note: Mercury (Hg) concentration, organic carbon isotope (δ^{13}C$_{org}$), mercury (Hg) mass-independent fractionation of odd Hg isotope (Δ^{199}Hg), mercury (Hg) mass-dependent fractionation (δ^{202}Hg), total organic carbon (TOC) concentration, total sulfur (TS) concentration, total clay minerals (TCM) concentration, mercury to total organic carbon (Hg/TOC), mercury to total sulfur (Hg/TS), and mercury to total clay minerals (Hg/TCM). VPDP—Vienna Pee Dee belemnite.

Clarification of mineral compositions and their paragenetic sequence in bauxite ore is essential to determine the depositional conditions (Temur and Kansun, 2006; Laskou and Economou-Eliopoulos, 2013; Wang et al., 2021). Alumina minerals in the bauxite ore from the NCB are dominated by diaspore with very little boehmite or gibbsite, and pyrite, siderite, goethite, chamosite, and berthierine are the main iron-bearing minerals (Table S1; Figs. 5A and 6A–6H; Liu et al., 2013, 2020). Nearly all the diaspores coexist with pyrite, siderite, anatase, chamosite, and berthierine in the NCB bauxite ore (Figs. 6A–6F; Liu et al., 2013, 2020; Zhao et al., 2021). Kaolinite and illite are the main clay minerals in the ore, and their occurrence suggests that they were mainly formed by early weathering (Fig. 6G; Liu, 2011). The above evidences suggest that the bauxite ore in the NCB formed in an alkaline and weak reducing karstic environment (D'Argenio and Mindszenty, 1995; Zarasvandi et al., 2008). Widespread framboidal pyrite with δ^{34}S value as low as −11.5‰ and microorganisms, and their intimate combinations with diaspore, denote microbial involvement in the bauxitization process (Liu et al., 2020; Figs. 6A and 6H).

Diaspore is the only alumina mineral in the Permian bauxite ore from YB and it closely coexists with pyrite, amesite, chamosite, bastnäsite, parisite, and anatase (Figs. 5B and 7A–7F; Liu et al., 2016). This reveals that the Permian bauxite ore in YB also precipitated under an alkaline and strong reducing
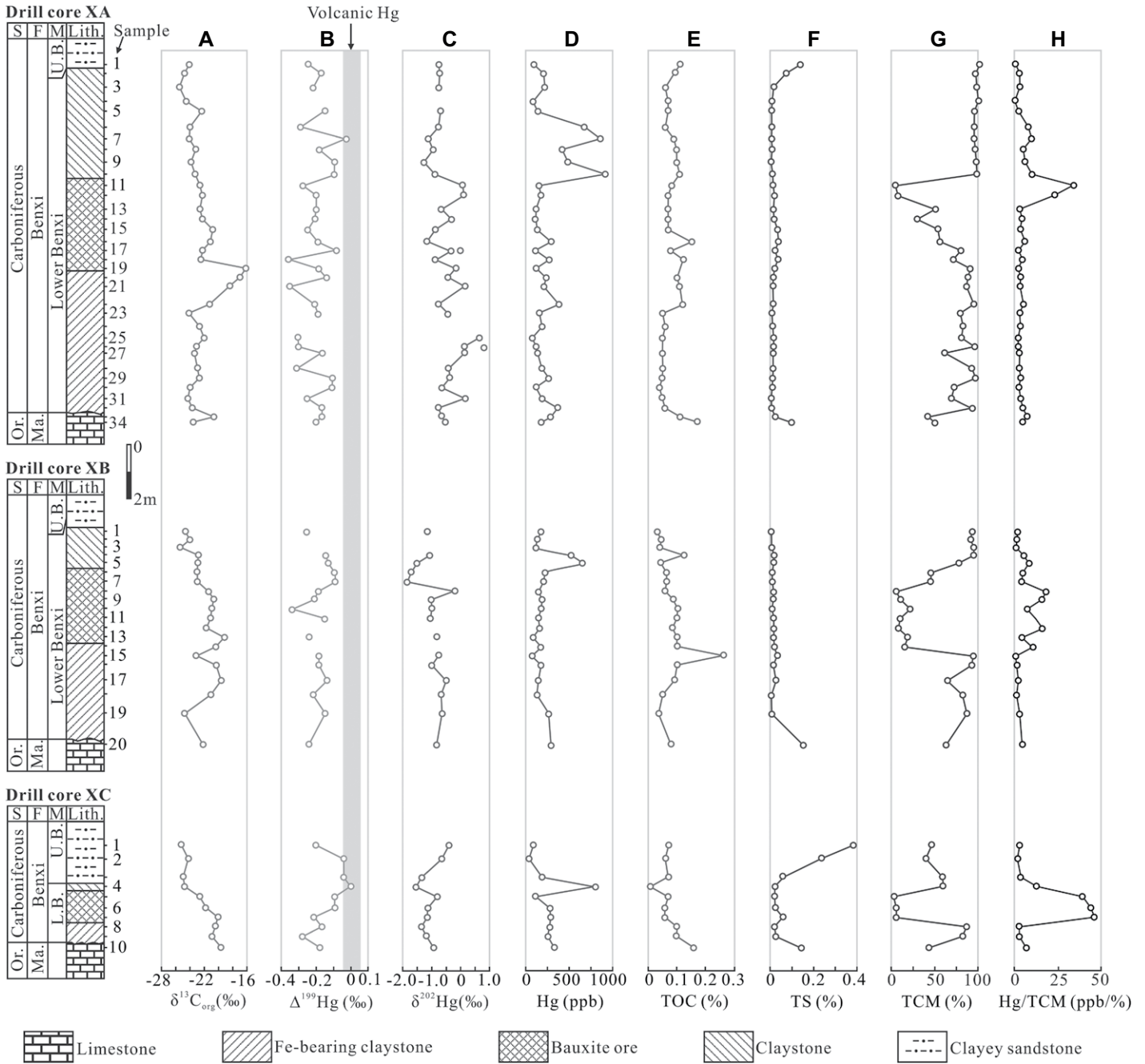
Figure 8. Profiles from drill core XA, XB, and XC of Xinxian bauxite deposit of China: (A) organic carbon isotope ($\delta^{13}C_{org}$); (B) mercury (Hg) mass-independent fractionation of odd Hg isotope ($\Delta^{199}Hg$); (C) mercury (Hg) mass-dependent fractionation ($\delta^{202}Hg$); (D) mercury (Hg) concentration; (E) total organic carbon (TOC) concentration; (F) total sulfur (TS) concentration; (G) total clay minerals (TCM) concentration; (H) mercury (Hg) versus TCM ratio. Vertical gray rectangle in column b is the range of volcanic $\Delta^{199}Hg$ (+0.02 ± 0.06‰; Yin et al., 2016). S—System; F—Formation; M—Member; Lith.—Lithos, Or.—Ordovician; Ma.—Majiagou; U.B.—Upper Benxi; L.B.—Lower Benxi.

karstic environment (D'Argenio and Mind-szenty, 1995; Temur and Kansun, 2006; Liu et al., 2016, 2017). Kaolinite and pyrophyllite are the two main clay minerals in the Gaoji deposit. According to their occurrence and relationship with other minerals, it is revealed that pyrophyllite, parisite, and diaspore were precipitated in the same period (Liu et al., 2016; Figs. 7E and 7F), and kaolinite is mainly the result of epigenetic diaspore silicification (Dangić, 1985, 1988; Figs. 7F–7H). Extensive development of framboidal pyrite hav-ing distinct negative $\delta^{34}S$ values (as low as −34.11‰), together with the widespread pres-ervation of microorganisms and organic mat-ters in the bauxite ore confirm the involvement of microbial activity in this bauxite formation (Yang et al., 2021).

TABLE 2. ANALYZED SAMPLES FROM THE TWO DRILL CORES OBTAINED FROM THE GAOJI BAUXITE DEPOSIT OF YOUJIANG BASIN OF CHINA

Sample	Hg (ppb)	δ^{202}Hg (‰)	Δ^{199}Hg (‰)	TOC (%)	δ^{13}C-VPDB (‰)	TS (%)	TCM (%)	Hg/TOC (ppb/%)	Hg/TS (ppb/%)	Hg/TCM (ppb/%)
GA-1	57	−1.07	0.22	1.29		0.28	14	44	204	4
GA-2	1893	0.73	−0.07	1.61	−25.10	11.88	21	1176	159	90
GA-3	642	−1.26	−0.02	1.57	−24.39	2.81	42	409	228	15
GA-4	2110	−2.54	0.07	13.98	−24.50	9.49	40	151	222	53
GA-5	1653	−2.53	0.01	1.17	−23.69	16.13	3	1413	102	551
GA-6	1380	−2.65	−0.01	1.21	−23.87	13.18	9	1140	105	153
GA-7	1042	−2.64	0.05	0.51	−23.74	10.74	0	2043	97	
GA-8	2170	−2.7	0	0.97	−23.86	18.92	0	2237	115	
GA-9	1321	−1.4	−0.07	1.84	−23.95	6.95	43	718	190	31
GA-10	1243	−1.35	−0.05	2.45	−24.04	5.70	43	507	218	29
GA-11	1761	−1.46	−0.04	1.13	−24.00	9.64	29	1558	183	61
GA-12	1349	−0.78	−0.06	1.88	−23.94	7.26	43	718	186	31
GA-13	1180	−0.86	−0.05	1.86	−24.09	6.74	53	634	175	22
GA-14	1143	−1.67	0.03	0.48	−23.75	8.51	7	2381	134	163
GA-15	890	−1.19	−0.1	1.08	−24.17	9.65	54	824	92	16
GA-16	1776	−1.59	0.02	0.44	−23.77	15.57	7	4036	114	254
GA-17	56	−0.04	−0.03	0.03			0	1867		
GA-18	54	0.07	−0.12	0.03			0	1800		
GA-19	49	0.04	−0.1	0.05	−26.05	13.74	0	980	4	
GB-1	3	−1.06	−0.04	0.07		5.99	0	43	1	
GB-2	2	−1.33	−0.01	0.11	−23.19	2.50	0	18	1	
GB-3	95	−0.55	−0.05	0.26	−22.83	2.40	63	365	40	2
GB-4	1572	−1.1	−0.04	2.1	−23.83	3.05	94	749	516	17
GB-5	377	−0.65	0.02	0.42	−22.87	4.40	61	898	86	6
GB-6	201	−1.04	0.1	1.55	−23.62	7.28	5	130	28	40
GB-7	188	−0.4	−0.01	0.66	−22.80	4.79	6	285	39	31
GB-8	1109	−0.41	−0.04	0.47	−22.89	3.45	8	2360	322	139
GB-9	99	−0.82	0.04	1.26	−23.06	5.71	6	79	17	17
GB-10	279	−0.77	0.05	1.75	−23.35	13.03	9	159	21	31
GB-11	132	−0.9	−0.02	1.95	−23.33	7.08	10	68	19	13
GB-12	160	−0.72	0.04	2.45	−23.37	9.46	11	65	17	15
GB-14	112	−0.89	0.07	1.12	−23.28	7.68	12	100	15	9
GB-15	99	−0.92	0.04	1.18	−23.01	7.39	10	84	13	10
GB-16	1104	−1.16	0.08	1.42	−23.41	6.61	8	777	167	138
GB-17	104	−0.84	0.03	1.03	−23.09	7.21	6	101	14	17
GB-18	114	−0.7	0.01	1.54	−23.29	7.53	9	74	15	13
GB-19	178	−0.78	0.05	0.62	−23.07	11.60	4	287	15	45
GB-20	1529	−0.76	0.03	0.81	−23.28	8.06	10	1888	190	153
GB-21	86	−0.53	0.1	0.75	−22.98	8.52	10	115	10	9
GB-22	95	−0.84	0.11	1.55	−23.12	4.02	5	61	24	19
GB-23	334	−0.91	0.03	1.09	−23.53	20.31	7	306	16	48
GB-24	172	−0.89	0.09	1.97	−23.31	7.45	9	87	23	19
GB-25	1737	−0.87	0.11	1.27	−23.32	10.76	2	1368	161	869
GB-26	16	−0.73	0.15	0.13			0	123		
GB-27	4	−1.04	0.07	0.05			0	80		
GB-28	76	−0.67	0.12	0.23	−24.18	30.08	0	330	3	

Note: Mercury (Hg) concentration, organic carbon isotope (δ^{13}C$_{org}$), mercury (Hg) mass-independent fractionation of odd Hg isotope (Δ^{199}Hg), mercury (Hg) mass-dependent fractionation (δ^{202}Hg), total organic carbon (TOC) concentration, total sulfur (TS) concentration, total clay minerals (TCM) concentration, mercury to total organic carbon (Hg/TOC), mercury to total sulfur (Hg/TS), and mercury to total clay minerals (Hg/TCM). VPDP—Vienna Pee Dee belemnite.

6.2. Host Phases of Hg and Extreme Enrichment in Bauxite Ore and Claystone

The use of Hg as a volcanic proxy requires an understanding of its sedimentary host phases (Shen et al., 2020). In marine sediments, Hg has been shown to have a high affinity for organic matter (OM) and reduced sulfur due to the formation of Hg-OM and Hg-S complexes. However, samples from the Xinxian bauxite deposit in the NCB are characterized by extremely low TOC and TS concentrations, therefore OM and sulfides do not seem to be the major host phases of Hg (Fig. 8; Grasby et al., 2019). This is also supported by the lack of correlation between Hg and TOC and between Hg and TS in the Xinxian samples (Figs. 10A–10F). Uniformly positive correlations between Hg and TCM were observed in these samples (Figs. 10G–10I), suggesting that clay minerals are the dominant hosts of Hg, as they can absorb large amounts of Hg (Farrah and Pickering, 1978; Kongchum et al., 2011; Shen et al., 2020).

In contrast to the Xinxian samples, the Permian Gaoji bauxite has higher concentrations of TS and TOC in the bauxite ore and claystone horizons (Table 2). In the GA drill core, Hg has a marked positive correlation with TS (r = +0.69, p > 0.05, n = 14) and a positive correlation with TOC (r = +0.39, p > 0.05, n = 14) (Figs. 11A and 11C). However, in the drill core GB, there is a positive correlation between Hg and TCM (r = +0.35, p > 0.05, n = 21) and a weaker positive correlation between Hg and TS (r = 0.12, p > 0.05, n = 21) (Figs. 11D and 11F). This result reveals the variability of Hg host phase in the Gaoji bauxite, but sulfide is the main one (Figs. 9 and 11).

Although both belong to karstic bauxite, the host phases of Hg in Xinxian bauxite of NCB and Gaoji bauxite of YB are different. This is mainly due to the different compositions and ore-forming conditions of the two deposits (Liu et al., 2017, 2020; Shen et al., 2020). Bauxite in Xinxian is rich in clay minerals, poor TOC and TS, and formed under alkaline and weak reduc-

ing conditions. Hg in the bauxite and claystone is thus mainly absorbed by the clay minerals. While bauxite in Gaoji of YB is highly enriched in TOC and TS, and formed under alkaline and intensely reducing conditions (Liu et al., 2017). Hg in the bauxite ore is thus mainly hosted in the sulfide. This result is consistent with the viewpoint in the marine sediments obtained by Shen et al. (2020), which proposed that a sulfide host phase is more likely in strongly euxinic depositional facies, as reflected in high TS concentrations (>1.0%) and TS/TOC ratios (>~0.35 ppb/%). The TS concentrations and TS/TOC ratios of both drill cores in Gaoji bauxite are far exceeding 0.1% and 0.35 ppb/%, respectively (Table 2).

The Hg enrichment in marine and terrestrial sediments (10^2 to 10^3 ppb) has been frequently reported, most of which are directly related to volcanic eruptions (Grasby et al., 2019; Shen et al., 2019c, 2020), and some of which are also related to the presence of Hg-rich sulfides (Shen et al., 2019b). This study observed extremely high Hg concentrations
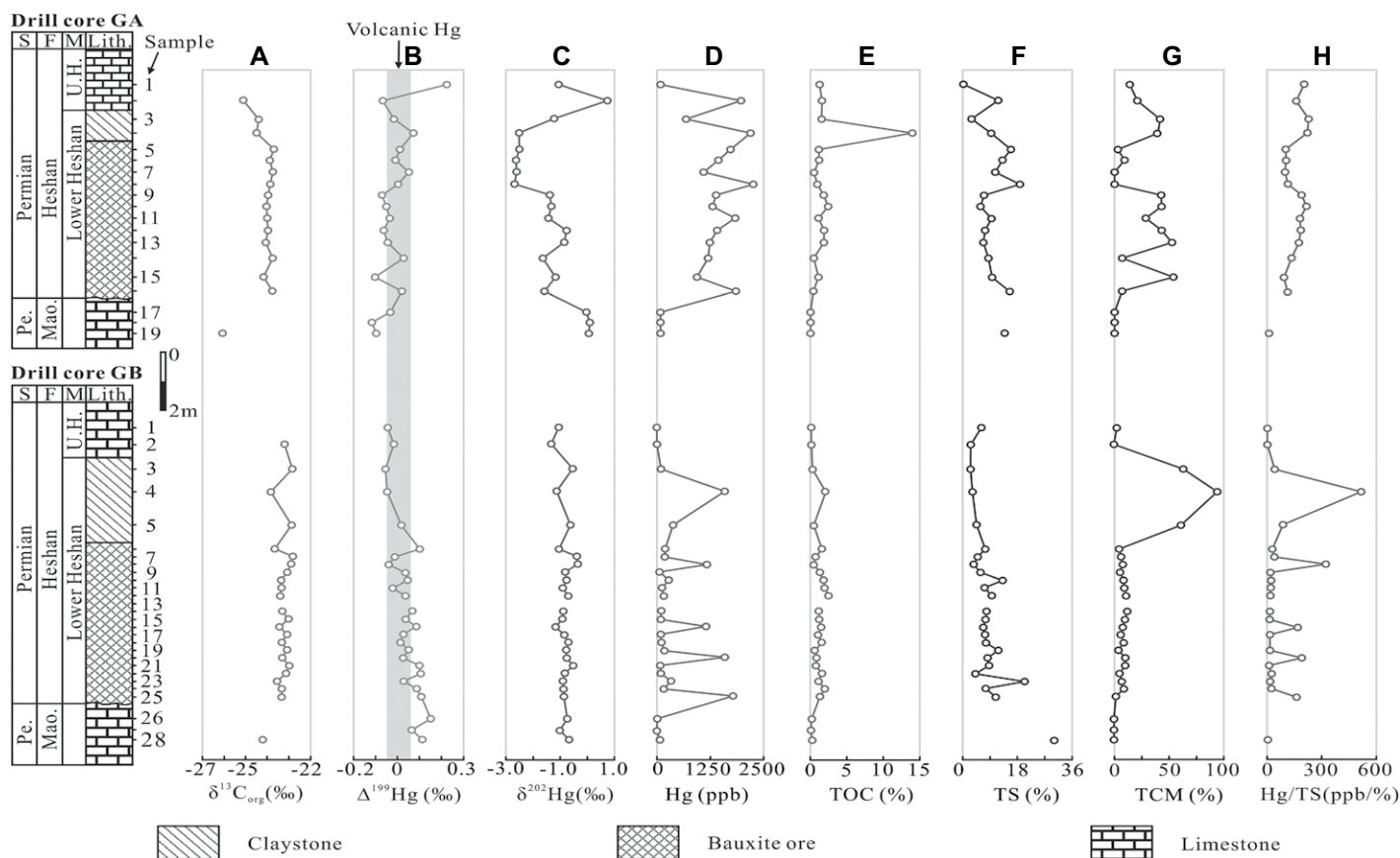
Figure 9. Profiles from drill core GA and GB of Gaoji bauxite deposit of China: (A) organic carbon isotope ($\delta^{13}C_{org}$); (B) mercury (Hg) mass-independent fractionation of odd Hg isotope ($\Delta^{199}Hg$); (C) mercury (Hg) mass-dependent fractionation ($\delta^{202}Hg$); (D) mercury (Hg) concentration; (E) total organic carbon (TOC) concentration; (F) total sulfur (TS) concentration; (G) total clay minerals (TCM) concentration; (H) mercury (Hg) versus total sulfur (TS) ratio. Vertical gray rectangle in column B is the range of volcanic $\Delta^{199}Hg$ (+0.02 ± 0.06‰; Yin et al., 2016). S—System; F—Formation; M—Member; Lith.—Lithos; Pe.—Permian; Mao.—Maokou; U.H.—Upper Heshan.

(up to 2000 ppb) in the bauxite ore in the NCB and YB (Table 2). Although some of the ores contain abundant pyrites, suggesting sulfides as important hosts of Hg, the very low TS content in most of these ores suggests the presence of large volcanism during the formation of bauxite deposits.

6.3. Variations in Hg Concentrations and Isotopes and their Implications for Bauxitization

Bauxite ore in NCB is mostly characterized by negative $\Delta^{199}Hg$ and lower Hg concentrations, while that in YB has near-zero $\Delta^{199}Hg$ and higher Hg concentrations (Figs. 8 and 9), suggesting different pathways of Hg entering the bauxite deposits.

6.3.1. Late Carboniferous Bauxite within the North China Basin

Previous studies have confirmed that the bauxite and claystone of NCB were transformed from the weathered residual soil of the igneous and metamorphic rocks at basin margins (Wang et al., 2016; Zhao and Liu, 2019). These terrestrial weathered soils were generally considered to be characterized by negative $\Delta^{199}Hg$ (Zhang et al., 2013; Yin et al., 2016), which agrees well with the negative $\Delta^{199}Hg$ values and lower Hg concentrations observed in the entire profile of three drill cores except for a thin horizon in the upper claystone (Fig. 8). The abrupt Hg-enriched peaks in the upper claystone layer that occurs uniformly in all three drill cores are indicative of excess Hg inputs during the Late Carboniferous, and the corresponding less negative to zero $\Delta^{199}Hg$, marks a rapid increase in volcanic Hg input because volcanic Hg is associated with near-zero $\Delta^{199}Hg$ (Fig. 8; Yin et al., 2016). Hg concentrations and $\Delta^{199}Hg$ values further confirm the transformation of bauxite from previously prepared soils and clays, and also reveal that volcanic activity was also involved in the formation of bauxite during the Late Carboniferous.

During the Late Carboniferous, the most likely place for large-scale volcanic activity in the NCB is on its northern margin, as extensive 320–300 Ma intrusions occurred along the northern margin, due to the subduction of the Paleo-Asian oceanic plate beneath the NCB (Zhang et al., 2007, 2009; Wang et al., 2018). Previous studies of detrital zircons from Late Carboniferous bauxite ore and claystone within the NCB have also suggested the possibility of large-scale volcanism along the northern margin of the NCB, but direct evidence has not yet been found (Liu et al., 2014; Wang et al., 2018). Identification of a Hg-enriched horizon in the Late Carboniferous bauxite and claystone and the corresponding positive shift in $\Delta^{199}Hg$ in this study supports the hypothesis of the extensive development of volcanism along the northern margin of the NCB during the Late Carboniferous. Magmas generated during the subduction of the Paleo-Asian oceanic plate migrated upward, were emplaced in the middle-upper crust, and erupted and formed extensive arc volcanoes.
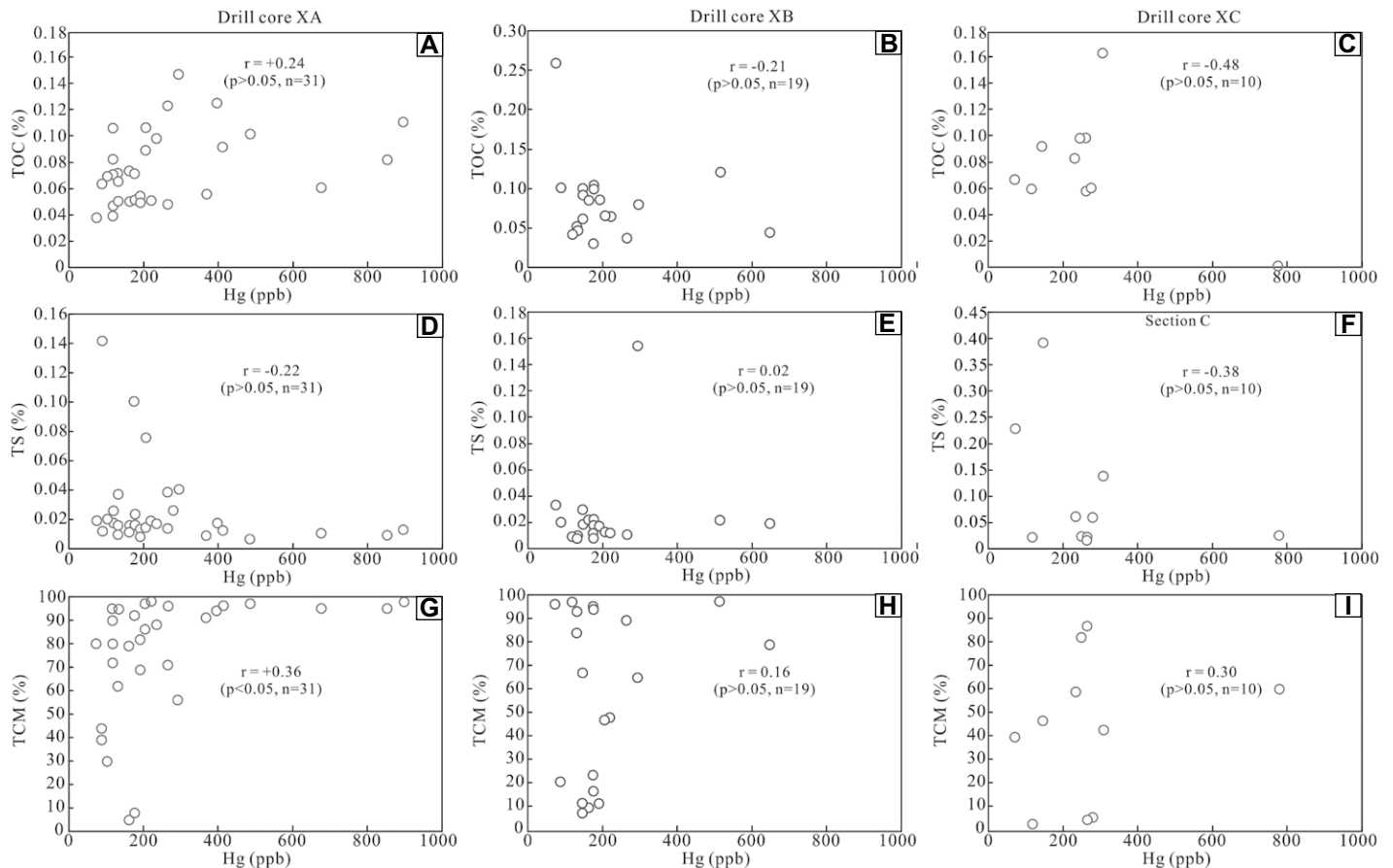
Figure 10. Cross-plots of Hg versus total organic carbon (TOC), Hg versus total sulfur (TS), and Hg versus total clay minerals (TCM) for the drill core XA (A, D, and G), drill core XB (B, E, and H), and drill core XC (C, F, and I) of Xinxian bauxite deposit of China, respectively.

The volcanic ash was transported southward by wind and streams and re-deposited in the karstic terrain. This is consistent with the widespread occurrence of 320–300 Ma volcanic zircons in the bauxite and claystone throughout the NCB (Liu et al., 2014; Wang et al., 2016; Zhao and Liu, 2019).

6.3.2. Late Permian Bauxite within the Youjiang Basin

The high Hg enrichments in the bauxite ore and claystone in both drill cores are also indicative of excess Hg inputs during the Late Permian in YB (Fig. 9). The near-zero $\Delta^{199}Hg$ values throughout the whole bauxite ore and claystone in the two drill cores denote volcanic Hg input during the entire bauxite formation process, given volcanic Hg has near-zero $\Delta^{199}Hg$ (Zambardi et al., 2009; Yin et al., 2016). In the Late Permian, the evident and extensive volcanism surrounding the YB comprised the Emeishan LIP, generated by a mantle plume (ca. 260 Ma) (Shellnutt and Zhou, 2007; Deng et al., 2010; He et al., 2010). Volcanism induced by Paleo-Pacific subduction may also have influenced the

formation of bauxite (Wang et al., 2020). Based on detrital zircon dating and Sr-Nd-Pb isotope analyses of the bauxite ore, igneous rocks generated in these eruptions are inferred to be the major source materials of the bauxite formation in the YB (Deng et al., 2010; Liu et al., 2017; Wang et al., 2020). The presence of marked Hg enrichment and near-zero $\Delta^{199}Hg$ values in the entirety of the bauxite ore and claystone horizons of this study proved that volcanism greatly affected the land surface and massive volcanic ashes were also deposited in the YB. Compared with the Hg-enriched horizon occurring only in the upper claystone layer, the Hg-enriched horizon throughout the whole bauxite ore and claystone layers denotes the intensity of volcanism induced by LIP in the YB is far greater than arc volcanoes along the northern margin of the NCB.

6.4. Intensive and Apace Bauxitization over the Paleo-Karstic Surface

Previous studies have suggested that diaspore-dominant karstic bauxite formed due to the transformation of early-formed gibbsite-rich

laterites over subsequent long metamorphic periods (Temur and Kansun, 2006; Hatipoğlu et al., 2010; Zarasvandi et al., 2012; Mongelli et al., 2016), because direct precipitation of diaspore from Al-rich solutions has rarely been observed at Earth surface conditions (Chesworth, 1978; Sidibe and Yalcin, 2019). However, there are several reports of the deposition of diaspore in karstic bauxite deposits at Earth surface conditions (Laskou and Economou-Eliopoulos, 2007, 2013; Liu et al., 2010, 2013, 2017, 2020; Sidibe and Yalcin, 2019). This genetic mechanism usually forms large-scale bauxite over the paleo-karstic surface within a short period of time. For example, ~5 billion tons of bauxite ore formed within 20 Ma in the NCB during the Late Carboniferous (Liu, 2011), and ~1 billion tons of bauxite ore formed within 10 Ma in the YB during the Late Permian (Zhang, 2011). These bauxite deposits are closely related to extensive volcanism. The Hg compositions and isotope data obtained in this study, together with the previous zircon U-Pb dating of bauxite ore (Wang et al., 2010; Liu et al., 2014; Wang et al., 2016: Zhao and Liu, 2019), have verified that
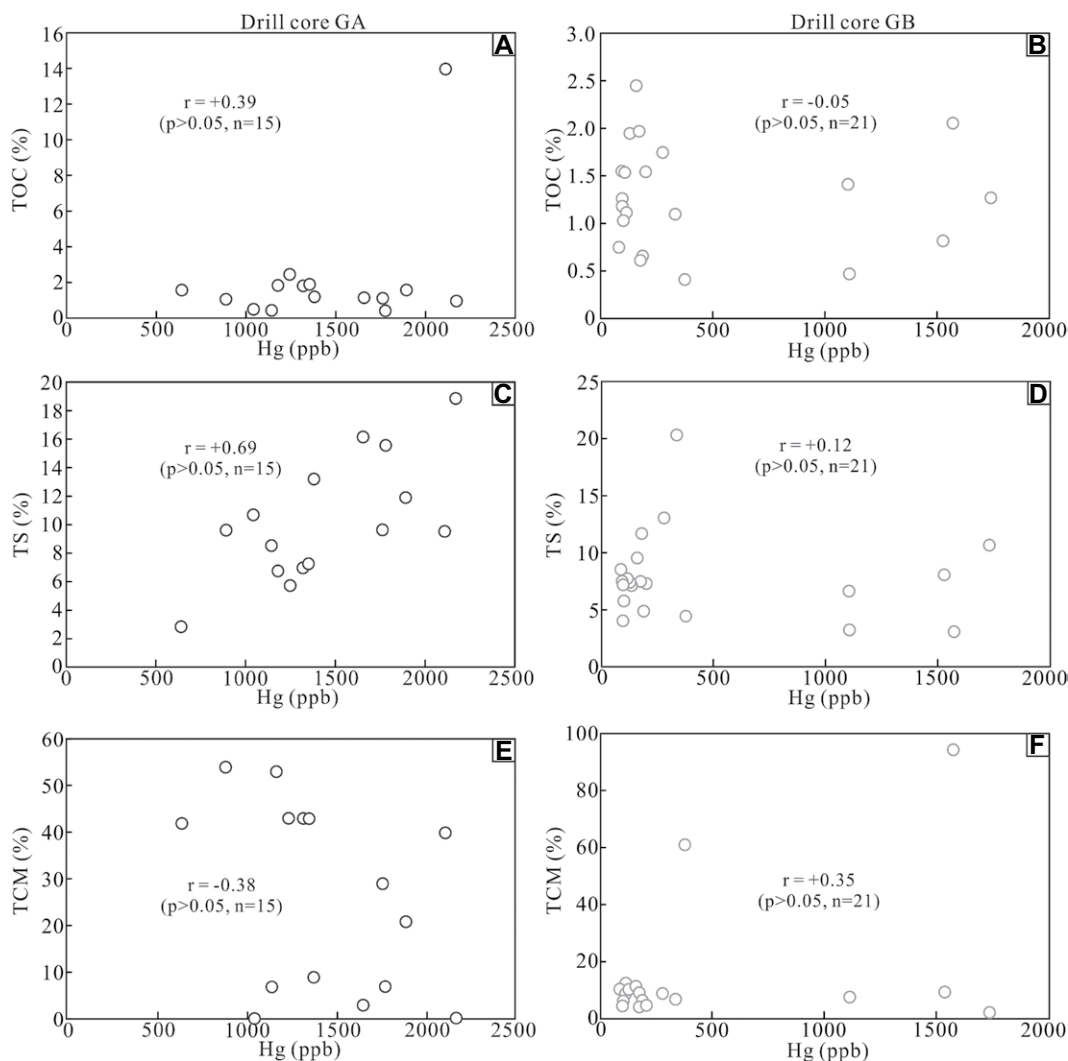
Figure 11. Cross-plots of Hg versus total organic carbon (TOC), Hg versus total sulfur (TS), and Hg versus total clay minerals (TCM) for the drill core XA (A, D, and G), drill core XB (B, E, and H), and drill core XC (C, F, and I) of Gaoji bauxite deposit of China, respectively.

extensive volcanism took place along the northern margin of the NCB in the Late Carboniferous. This volcanism accelerated the weathering of long-term accumulated Al-rich remnants via subsequent surface climate change. The Permian karstic bauxite deposits in the YB are here

confirmed to be mainly related to the eruption of the Emeishan LIP, which not only provided sufficient source material for bauxite formation, but also accelerated the weathering and dissociation of source materials (Deng et al., 2010; Liu et al., 2017).

Based on the achievements of this study, together with previous studies on the genesis of bauxite in the NCB and YB by Deng et al. (2010), Liu et al. (2013, 2017, 2020), Yu et al. (2016, 2019), and Wang et al. (2016, 2020), volcanic effect on the apace and intensified bauxite
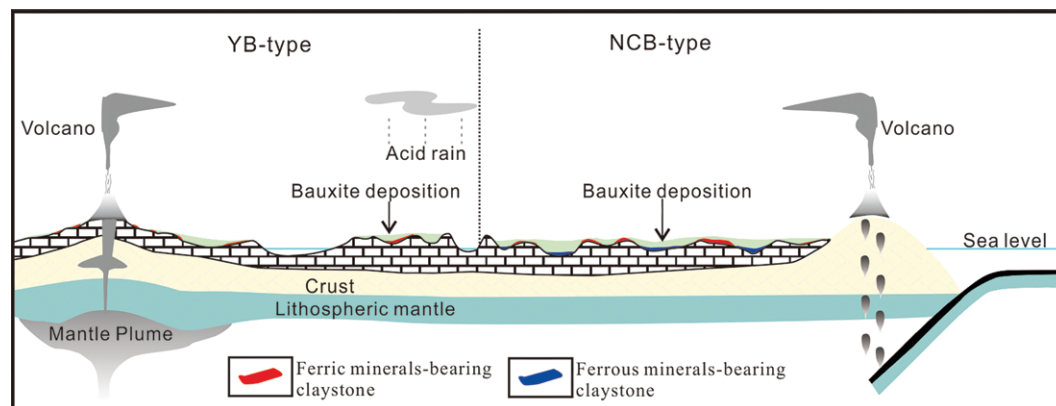
Figure 12. A conceptual model diagram illustrating the formation mechanism of Hg-enriched bauxite and claystone in the North China Basin (NCB-type) and Yongjiang Basin (YB-type) of China.

formation process over the paleo-karstic terrain in the NCB and YB were clarified (Fig. 12).

The conceptual model of Carboniferous bauxite in NCB is shown in Figure 12 (i.e., NCB-type). The accretion of the North Qinling arc terrane to the southern margin of the NCB during the Late Carboniferous induced the northward-dipping topography of the NCB and the subsequent input of weathered material from the North Qinling arc terrane to the NCB (Wang et al., 2016). The subduction of the Paleo-Asian oceanic plate along the northern margin of NCB led to its uplift and the concomitant developments of arc intrusions and volcanoes at Late Carboniferous (320–300 Ma) (Fig. 12). Weathered materials from the northern margin of NCB were transported into the interior of NCB (Wang et al., 2016; Zhao et al., 2021), and the volcanic ash was also transported southward by wind and streams and re-deposited in the karstic terrain (Fig. 12). Extensive arc volcanism subsequent to the accumulation of long-term weathered remnants resulted in spikes in emissions of carbon dioxide, methane, sulfur, mercury, and chlorine (Svensen et al., 2009; Sanei et al., 2012; Black et al., 2018), together with high Earth surface temperatures (Joachimski et al., 2012), intense continental weathering (Sephton et al., 2005; Algeo and Twitchett, 2010), and acid rain (Wang et al., 2018), which accelerated the weathering and dissociation of near-surface materials in acidic and oxidizing conditions throughout the whole NCB (Fig. 12). Released ions (i.e., Al^{3+}, Ti^{4+}, and Fe^{3+}) eluviated downward and encountered alkaline and reducing conditions near the karstic surface to precipitate diaspore, anatase, pyrite, siderite, berthierine, and chamosite (Laskou and Economou-Eliopoulos, 2013; Liu et al., 2020). Approximately 5 billion tons of bauxite ore were formed in the Late Carboniferous between 320 and 300 Ma.

The conceptual model of Permian bauxite in YB is shown in Figure 12 (i.e., YB-type). Western Guangxi was uplifted at the end of the middle Permian and suffered extensive weathering and karstification; thin Fe-bearing claystone and/or weathered iron ore were thus formed during a transient period (Fig. 4B; He et al., 2010; Liu et al., 2017). At ca. 260 Ma, the eruption of the Emeishan LIP resulted in volcanic lava and ash covering or infilling the paleo-karstic surface (Yu et al., 2019). Volcanism related to the Paleo-Pacific subduction also provided a certain source of material (Wang et al., 2020). Volcanic eruptions during this period dramatically changed the surface environment. Under strong acidic conditions and extensive bacterial and microbial activity, previously formed Fe-bearing claystone as well as volcanic lava and ash were completely weathered and decomposed. Subsequently, with the rise of groundwater, an alkaline and strong reducing karstic environment appeared on the surface of Maokou limestone, forming a large amount of diaspore, pyrite, diabase, amesite, and anatase (Liu et al., 2017). Due to intense weathering induced by volcanic activity, the bauxite ore directly covered the Maokou limestone karstic surface in most areas (Liu et al., 2017; Figs. 4A and 4D), abundant rare earth element fluorocarbonates (such as parisite and bastnäsite) also precipitated near the karstic surface (Liu et al., 2016). Approximately one billion tons of bauxite ore were formed between 260 and 250 Ma.

Despite the Carboniferous karstic bauxite in the NCB and the Permian karstic bauxite in YB being formed in different tectonic units and times, they share a similar formation mechanism. Karstic bauxite deposits of this genetic mechanism commonly share the following attributes: (1) they are closely related to contemporaneous volcanism; (2) they require an alkaline and reducing karstic environment for precipitation of diaspore near the surface; (3) microorganisms are widely preserved and play an important role in the bauxite formation process (Laskou and Economou-Eliopoulos, 2013; Liu et al., 2017, 2020). Volcanic eruptions along the northern margin of NCB caused rapid bauxitization of the long-term weathered Al-rich materials in the whole basin, while volcanism around the YB led to short-term weathering and apace bauxitization. This study clarifies the volcanic effect on the intensified and apace bauxitization over the paleo-karstic surface and updates the understanding of the genesis of global karstic bauxite.

7. CONCLUSIONS

Mineral assemblages in bauxite ore of the NCB (i.e., diaspore, pyrite, anatase, siderite, berthierine, and chamosite) and YB (i.e., diaspore, pyrite, chamosite, amesite, anatase, bastnäsite, and parisite) confirm that they were deposited in alkaline and reducing karstic environments.

From all three drill cores in the Xinxian deposit in NCB, Hg in the bauxite ore and claystone here was mainly adsorbed by the clay minerals. Marked Hg enrichment peaks and corresponding near-zero $\Delta^{199}Hg$ in the upper claystone indicate that extensive volcanism immediately affected the land surface of the NCB subsequent to the deposition of long-term weathered Al-rich remnants during Late Carboniferous; this volcanism occurring along the northern margin of the NCB led to apace bauxitization of the prepared Al-rich remnants in the whole NCB.

In the YB, the host phase of Hg in the bauxite ore and claystone at Gaoji is variable. Strong Hg enrichment and uniform near-zero $\Delta^{199}Hg$ throughout bauxite ore and claystone layers confirm that volcanism was involved in the entire bauxite formation; this volcanism associated with the Emeishan LIP and contemporaneous arc system resulted in short-term weathering and apace bauxitization in the YB.

Volcanism is approved to cause intensified and apace bauxitization over the paleo-karstic surface. It can accelerate the weathering and dissolution of parent rocks by changing the surface environment. Released ions (i.e., Al^{3+}, Ti^{4+}, Fe^{3+}, REE^{4+}) eluviated downward and encountered alkaline and reducing conditions near the carbonate barrier, forming large-scale bauxite ores.

REFERENCES CITED

Abedini, A., Mongelli, G., and Khosravi, M., 2021, Geochemical constraints on the middle Triassic Kani Zarrineh karst bauxite deposit, Irano–Himalayan belt, NW Iran: Implications for elemental fractionation and parental affinity: Ore Geology Reviews, v. 133, https://doi.org/10.1016/j.oregeorev.2021.104099.

Algeo, T.J., and Twitchett, R.J., 2010, Anomalous Early Triassic sediment fluxes due to elevated weathering rates and their biological consequences: Geology, v. 38, p. 1023–1026, https://doi.org/10.1130/G31203.1.

Bárdossy, G., 1982, Karst bauxites, bauxite deposits on carbonate rocks: Developments in Economic Geology, 441 p.

Bárdossy, G., and Combes, J., 1999, Karst bauxites: Interfingering of deposition and paleoweathering: Special Publication of the International Association of Sedimentologists, v. 27, p. 189–206.

Bergquist, B.A., and Blum, J.D., 2007, Mass-dependent and -independent fractionation of Hg isotopes by photoreduction in aquatic systems: Science, v. 318, p. 417–420, https://doi.org/10.1126/science.1148050.

Bishop, M.E., Dong, H., Kukkadapu, R.K., Liu, C., and Edelmann, R.E., 2011, Bioreduction of Fe-bearing clay minerals and their reactivity toward pertechnetate (Tc-99): Geochimica et Cosmochimica Acta, v. 75, p. 5229–5246, https://doi.org/10.1016/j.gca.2011.06.034.

Black, B.A., Neely, R.R., Lamarque, J.F., Elkins-Tanton, L.T., Kiehl, J.T., Shields, C.A., Mills, M.J., and Bardeen, C., 2018, Systemic swings in end-Permian climate from Siberian Traps carbon and sulfur outgassing: Nature Geoscience, v. 11, p. 949–954, https://doi.org/10.1038/s41561-018-0261-y.

Bogatyrev, B.A., Zhukov, V.V., and Tsekhovsky, Y.G., 2009, Formation conditions and regularities of the distribution of large and superlarge bauxite deposits: Lithology and Mineral Resources, v. 44, p. 135–151, https://doi.org/10.1134/S0024490209020035.

Cai, J.X., and Zhang, K.J., 2009, A new model for the Indochina and South China collision during the late Permian to the middle Triassic: Tectonophysics, v. 467, p. 35–43, https://doi.org/10.1016/j.tecto.2008.12.003.

Chesworth, W., 1978, Discussion: A working model of some equilibria in the system alumina-silica-water: American Journal of Science, v. 278, p. 1018–1023, https://doi.org/10.2475/ajs.278.7.1018.

Chung, S.L., and Jahn, B.M., 1995, Plume-lithosphere interaction in generation of the Emeishan flood basalts at the Permian–Triassic boundary: Geology, v. 23, p. 889–892, https://doi.org/10.1130/0091-7613(1995)023<0889:PLIIGO>2.3.CO;2.

D'Argenio, B., and Mindszenty, A., 1995, Bauxites and related paleokarst: tectonic and climatic event markers at regional unconformities: Eclogae Geologicae Helvetiae, v. 88, p. 453–499.

Dangić, A., 1985, Kaolinization of bauxite: A study in the Vlasenice bauxite area, Yugoslavia. I. Alteration of matrix: Clays and Clay Minerals, v. 33, no. 6, p. 517–524, https://doi.org/10.1346/CCMN.1985.0330606.

Dangić, A., 1988, Kaolinization of bauxite: A study of the Vlasenice bauxite area, Yugoslavia. II. Alteration of oolites: Clays and Clay Minerals, v. 36, no. 5, p. 439–447, https://doi.org/10.1346/CCMN.1988.0360509.

Deng, C.Z., Sun, G.Y., Rong, Y.M., Sun, R.Y., Sun, D.Y., Lehmann, B., and Yin, R.S., 2021a, Recycling of mercury from the atmosphere-ocean system into volcanic-arc–associated epithermal gold systems: Geology, v. 49, p. 309–313, https://doi.org/10.1130/G48132.1.

Deng, J., and Wang, Q.F., 2016, Gold mineralization in China: Metallogenic provinces, deposit types and tectonic framework: Gondwana Research, v. 36, p. 219–274, https://doi.org/10.1016/j.gr.2015.10.003.

Deng, J., Wang, Q.F., Yang, S.J., Liu, X.F., Zhang, Q.Z., Yang, L.Q., and Yang, Y.H., 2010, Genetic relationship between the Emeishan plume and the bauxite deposits in Western Guangxi, China: Constraints from U-Pb and Lu-Hf isotopes of the detrital zircons in bauxite ores: Journal of Asian Earth Sciences, v. 37, p. 412–424, https://doi.org/10.1016/j.jseaes.2009.10.005.

Deng, J., Wang, Q.F., Li, G.J., and Santosh, M., 2014, Cenozoic tectono-magmatic and metallogenic processes in the Sanjiang region, southwestern China: Earth-Science Reviews, v. 138, p. 268–299, https://doi.org/10.1016/j.earscirev.2014.05.015.

Deng, J., Wang, C.M., Bagas, L., Santosh, M., and Yao, E.Y., 2018, Crustal architecture and metallogenesis in the south-eastern North China Craton: Earth-Science Reviews, v. 182, p. 251–272, https://doi.org/10.1016/j.earscirev.2018.05.001.

Deng, J., Wang, Q.F., Gao, L., He, W.Y., Yang, Z.Y., Zhang, S.H., Chang, L.J., Li, G.J., Sun, X., and Zhou, D.Q., 2021b, Differential crustal rotation and its control on giant ore clusters along the eastern margin of Tibet: Geology, v. 49, p. 428–432, https://doi.org/10.1130/G47855.1.

Du, Y.S., Huang, H.W., Huang, Z.Q., Xu, Y.J., Yang, J.H., and Huang, H., 2009, Basin translation from late Paleozoic to Triassic of Youjiang Basin and its tectonic significance [in Chinese with English abstract]: Bulletin of Geological Science and Technology, v. 286, p. 10–15.

Farrah, H., and Pickering, W.F., 1978, The sorption of mercury species by clay minerals: Water, Air, and Soil Pollution, v. 9, p. 23–31, https://doi.org/10.1007/BF00185744.

Grasby, S.E., Shen, W.J., Yin, R.S., Gleason, J.D., Blum, J.D., Lepak, R.F., Hurley, J.P., and Beauchamp, B., 2017, Isotopic signatures of mercury contamination in latest Permian oceans: Geology, v. 45, p. 55–58, https://doi.org/10.1130/G38487.1.

Grasby, S.E., Them, T.R., Chen, Z., Yin, R.S., and Ardakani, O.H., 2019, Mercury as a proxy for volcanic emissions in the geologic record: Earth-Science Reviews, v. 196, https://doi.org/10.1016/j.earscirev.2019.102880.

Hatipoğlu, M., Turk, N., Chamberlain, S.C., and Akgun, A.M., 2010, Gem-quality transparent diaspore (zultanite) in bauxite deposits of the degrees Ibir Mountains, Menderes Massif, SW Turkey: Mineralium Deposita, v. 45, p. 201–205, https://doi.org/10.1007/s00126-009-0262-2.

He, B., Xu, Y.G., Guan, J.P., and Zhong, Y.T., 2010, Paleokarst on the top of the Maokou Formation: Further evidence for domal crustal uplift prior to the Emeishan flood volcanism: Lithos, v. 119, p. 1–9, https://doi.org/10.1016/j.lithos.2010.07.019.

Hillier, S., 2000, Accurate quantitative analysis of clay and other minerals in sandstones by XRD: Comparison of a Rietveld and a reference intensity ratio (RIR) method and the importance of sample preparation: Clay Minerals, v. 35, p. 291–302, https://doi.org/10.1180/000985500546666.

Hou, Y.L., Zhong, Y.T., Xu, Y.G., and He, B., 2017, The provenance of late Permian karstic bauxite deposits in SW China, constrained by the geochemistry of interbedded clastic rocks, and U-Pb-Hf-O isotopes of detrital zircon: Lithos, v. 278–281, p. 240–254, https://doi.org/10.1016/j.lithos.2017.01.013.

Joachimski, M.M., Lai, X.L., Shen, S.Z., Jiang, H.S., Luo, G.M., Chen, B., Chen, J., and Sun, Y.D., 2012, Climate warming in the latest Permian and the Permian-Triassic mass extinction: Geology, v. 40, p. 195–198, https://doi.org/10.1130/G32707.1.

Kelemen, P., Dunkl, I., Csillag, G., Mindszenty, A., von Eynatten, H., and Józsa, S., 2017, Tracing multiple resedimentation on an isolated karstified plateau: The bauxite-bearing Miocene red clay of the Southern Bakony Mountains, Hungary: Sedimentary Geology, v. 358, p. 84–96, https://doi.org/10.1016/j.sedgeo.2017.07.005.

Kongchum, M., Hudnall, W.H., and Delaune, R.D., 2011, Relationship between sediment clay minerals and total mercury: Journal of Environmental Science and Health. Part A, Toxic/Hazardous Substances & Environmental Engineering, v. 46, p. 534–539, https://doi.org/10.1080/10934529.2011.551745.

Laskou, M., and Economou-Eliopoulos, M., 2007, The role of microorganisms on the mineralogical and geochemical characteristics of the Parnassos-Ghiona bauxite deposits, Greece: Journal of Geochemical Exploration, v. 93, p. 67–77, https://doi.org/10.1016/j.gexplo.2006.08.014.

Laskou, M., and Economou-Eliopoulos, M., 2013, Bio-mineralization and potential biogeochemical processes in bauxite deposits: Genetic and ore quality significance: Mineralogy and Petrology, v. 107, p. 471–486, https://doi.org/10.1007/s00710-012-0257-z.

Li, S.Z., Zhao, S.J., Liu, X., Cao, H.H., Yu, S., Li, X.Y., Somerville, I.D., Yu, S.Y., and Suo, Y.H., 2018, Closure of the Proto-Tethys Ocean and early Paleozoic amalgamation of microcontinental blocks in East Asia: Earth-Science Reviews, v. 186, p. 37–75, https://doi.org/10.1016/j.earscirev.2017.01.011.

Liu, J., Zhao, Y., Liu, A.K., Zhang, S.H., Yang, Z.Y., and Zhuo, S.G., 2014, Origin of Late Palaeozoic bauxites in the North China Craton: Constraints from zircon U-Pb geochronology and in situ Hf isotopes: Journal of the Geological Society, v. 171, p. 695–707, https://doi.org/10.1144/jgs2013-074.

Liu, X.F., 2011, Material composition and ore-forming process of bauxite (clay) deposits in western Henan, China [Ph.D. dissertation]: Beijing, China, China University of Geosciences, p. 1–176.

Liu, X.F., Wang, Q.F., Deng, J., Zhang, Q.Z., Sun, S.L., and Meng, J.Y., 2010, Mineralogical and geochemical investigations of the Dajia Salento-type bauxite deposits, western Guangxi, China: Journal of Geochemical Exploration, v. 105, p. 137–152, https://doi.org/10.1016/j.gexplo.2010.04.012.

Liu, X.F., Wang, Q.F., Feng, Y.W., Li, Z.M., and Cai, S.H., 2013, Genesis of the Guangou karstic bauxite deposit in western Henan, China: Ore Geology Reviews, v. 55, p. 162–175, https://doi.org/10.1016/j.oregeorev.2013.06.002.

Liu, X.F., Wang, Q.F., Zhang, Q.Z., Zhang, Y., and Li, Y., 2016, Genesis of REE minerals in the karstic bauxite in western Guangxi, China, and its constraints on the deposit formation conditions: Ore Geology Reviews, v. 75, p. 100–115, https://doi.org/10.1016/j.oregeorev.2015.12.015.

Liu, X.F., Wang, Q.F., Zhang, Q.Z., Yang, S.J., Liang, Y.Y., Zhang, Y., Li, Y., and Guan, T., 2017, Genesis of the Permian karstic Pingguo bauxite deposit, western Guangxi, China: Mineralium Deposita, v. 52, p. 1031–1048, https://doi.org/10.1007/s00126-017-0723-y.

Liu, X.F., Wang, Q.F., Zhao, L.H., Peng, Y.B., Ma, Y., and Zhou, Z.H., 2020, Metallogeny of the large-scale Carboniferous karstic bauxite in the Sanmenxia area, southern part of the North China Craton, China: Chemical Geology, v. 556, https://doi.org/10.1016/j.chemgeo.2020.119851.

Mei, M.X., Ma, Y.S., Deng, J., Chu, H.M., and Zheng, K.B., 2007, Sequence stratigraphic succession and paleogeography of the Yunnan–Guizhou–Guangxi and adjacent region [in Chinese with English abstract]: Science in China. Series D, Earth Sciences, v. 37, p. 605–617.

Mondillo, N., Herrington, R., and Boni, M., 2021, Bauxites, *in* Encyclopedia of Geology (Second Edition): London, UK, Academic Press, p. 694–707.

Mongelli, G., Boni, M., Buccione, R., and Sinisi, R., 2014, Geochemistry of the Apulian karst bauxites (southern Italy): Chemical fractionation and parental affinities: Ore Geology Reviews, v. 63, p. 9–21, https://doi.org/10.1016/j.oregeorev.2014.04.012.

Mongelli, G., Buccione, R., Gueguen, E., Langone, A., and Sinisi, R., 2016, Geochemistry of the apulian allochthonous karst bauxite, Southern Italy: Distribution of critical elements and constraints on Late Cretaceous Peri-Tethyan palaeogeography: Ore Geology Reviews, v. 77, p. 246–259, https://doi.org/10.1016/j.oregeorev.2016.03.002.

Mongelli, G., Mameli, P., Sinisi, R., Buccione, R., and Oggiano, G., 2021, Rees and other critical raw materials in Cretaceous Mediterranean-type bauxite: The case of the Sardinian ore (Italy): Ore Geology Reviews, v. 139, https://doi.org/10.1016/j.oregeorev.2021.104559.

Radusinović, S., Jelenković, R., Pačevski, A., Simić, V., Božović, D., Holclajtner-Antunović, I., and Životić, D., 2017, Content and mode of occurrences of rare earth elements in the Zagrad karstic bauxite deposit (Nikšić area, Montenegro): Ore Geology Reviews, v. 80, p. 406–428, https://doi.org/10.1016/j.oregeorev.2016.05.026.

Sanei, H., Grasby, S.E., and Beauchamp, B., 2012, Latest Permian mercury anomalies: Geology, v. 40, p. 63–66, https://doi.org/10.1130/G32596.1.

Selin, N.E., 2009, Global biogeochemical cycling of mercury: A review: Annual Review of Environment and Resources, v. 34, p. 43–63, https://doi.org/10.1146/annurev.environ.051308.084314.

Sephton, M.A., Looy, C.V., Brinkhuis, H., Wignall, P.B., de Leeuw, J.W., and Visscher, H., 2005, Catastrophic soil erosion during the end-Permian biotic crisis: Geology, v. 33, p. 941–944, https://doi.org/10.1130/G21784.1.

Shellnutt, J.G., and Zhou, M.F., 2007, Permian peralkaline, peraluminous and metaluminous A-type granites in the Panxi district, SW China: Their relationship to the Emeishan mantle plume: Chemical Geology, v. 243, p. 286–316, https://doi.org/10.1016/j.chemgeo.2007.05.022.

Shen, J., Chen, J., Algeo, T.J., Yuan, S., Feng, Q., Yu, J., Zhou, L., O'Connell, B., and Planavsky, N.J., 2019a, Evidence for a prolonged Permian–Triassic extinction interval from global marine mercury records: Nature Communications, v. 10, no. 1563, https://doi.org/10.1038/s41467-019-09620-0.

Shen, J., Algeo, T.J., Chen, J.B., Planavsky, N.J., Feng, Q.L., Yu, J.X., and Liu, J.L., 2019b, Mercury in marine Ordovician-Silurian boundary sections of South China is sulfide hosted and non-volcanic in origin: Earth and Planetary Science Letters, v. 511, p. 130–140, https://doi.org/10.1016/j.epsl.2019.01.028.

Shen, J., Algeo, T.J., Planavsky, N.J., Yu, J.X., Feng, Q.L., Song, H.J., Song, H.Y., Rowe, H., Zhou, L., and Chen, J.B., 2019c, Mercury enrichments provide evidence of Early Triassic volcanism following the end-Permian mass extinction: Earth-Science Reviews, v. 195, p. 191–212, https://doi.org/10.1016/j.earscirev.2019.05.010.

Shen, J., Yin, R.S., Zhang, S., Algeo, T., Bottjer, D.J., Yu, J.X., Xu, G.Z., Penman, D., Wang, Y.D., Li, L.Q., Shi, X., Planavsky, N., Feng, Q.L., and Xie, S.C., 2022, Intensified continental chemical weathering and carbon-cycle perturbations linked to volcanism during the Triassic–Jurassic transition: Nature Communications, v. 13, no. 299, https://doi.org/10.1038/s41467-022-27965-x.

Shen, X., Feng, Q.L., Algeo, T.J., Liu, J.L., Zhou, C.Y., Wei, W., Liu, J.S., Them, T.R., II, Gill, B.C., and Chen, J.B., 2020, Sedimentary host phases of mercury (Hg) and implications for use of Hg as a volcanic proxy: Earth and Planetary Science Letters, v. 543, https://doi.org/10.1016/j.epsl.2020.116333.

Sidibe, M., and Yalcin, M.G., 2019, Petrography, mineralogy, geochemistry and genesis of the Balaya bauxite deposits in Kindia region, Maritime Guinea, West Africa: Journal of African Earth Sciences, v. 149, p. 348–366, https://doi.org/10.1016/j.jafrearsci.2018.08.017.

Svensen, H., Planke, S., Polozov, A.G., Schmidbauer, N., Corfu, F., Podladchikov, Y.Y., and Jamtveit, B., 2009, Siberian gas venting and the end-Permian environmental crisis: Earth and Planetary Science Letters, v. 277, p. 490–500, https://doi.org/10.1016/j.epsl.2008.11.015.

Temur, S., and Kansun, G., 2006, Geology and petrography of the Masatdagi diasporic bauxites, Alanya, Antalya, Turkey: Journal of Asian Earth Sciences, v. 27, p. 512–522, https://doi.org/10.1016/j.jseaes.2005.07.001.

Thibodeau, A.M., Ritterbush, K., Yager, J.A., West, A.J., Ibarra, Y., Bottjer, D.J., Berelson, W.M., Bergquist, B.A., and Corsetti, F.A., 2016, Mercury anomalies and the timing of biotic recovery following the end-Triassic mass extinction: Nature Communications, v. 7, https://doi.org/10.1038/ncomms11147.

Valeton, I., 1972, Bauxites. Developments in Soil Science: Amsterdam, Netherlands, Elsevier, 226 p.

Veevers, J.J., 2004, Gondwanaland from 650–500 Ma assembly through 320 Ma merger in Pangea to 185–100 Ma breakup: Supercontinental tectonics via stratigraphy and radiometric dating: Earth-Science Reviews, v. 68, p. 1–132, https://doi.org/10.1016/j.earscirev.2004.05.002.

Wang, Q.F., Deng, J., Liu, X.F., Zhao, R., and Cai, S.H., 2016, Provenance of Late Carboniferous bauxite deposits in the North China Craton: New constraints on marginal arc construction and accretion processes: Gondwana Research, v. 38, p. 86–98, https://doi.org/10.1016/j.gr.2015.10.015.

Wang, Q.F., Yang, L., Xu, X.J., Santosh, M., Wang, Y.N., Wang, T.Y., Chen, F.G., Wang, R.X., Gao, L., Liu, X.F., Yang, S.J., Zeng, Y.C., Chen, J.H., Zhang, Q.Z., and Deng, J., 2020, Multi-stage tectonics and Metallogeny associated with Phanerozoic evolution of the South China Block: A holistic perspective from the Youjiang Basin: Earth-Science Reviews, v. 211, https://doi.org/10.1016/j.earscirev.2020.103405.

Wang, R.X., Wang, Q.F., Uysal, T., Ramanaidou, E., Deng, J., Todd, A., Verrall, M., and Liu, X.F., 2021, Mesozoic hydrothermal overprint on Carboniferous bauxite in China: Economic Geology, v. 116, p. 787–800, https://doi.org/10.5382/econgeo.4796.

Wang, Y., Zhou, L., Zhao, L., Ji, M., and Gao, H., 2010, Paleozoic uplands and unconformity in the North China Block: Constraints from zircon LA-ICP-MS dating and geochemical analysis of Bauxite: Terra Nova, v. 22, p. 264–273.

Wang, Y., Zhou, L.Y., Liu, S.F., Li, J.Y., and Yang, T.N., 2018, Post-cratonization deformation processes and tectonic evolution of the North China Craton: Earth-Science Reviews, v. 177, p. 320–365, https://doi.org/10.1016/j.earscirev.2017.11.017.

Xu, Y.G., Chung, S.L., Jahn, B.M., and Wu, J.Y., 2001, Petrologic and geochemical constraints on the petrogenesis of Permian–Triassic Emeishan flood basalts in southwestern China: Lithos, v. 58, p. 145–168, https://doi.org/10.1016/S0024-4937(01)00055-X.

Yang, S.J., Wang, Q.F., Lai, X.L., Qiao, L., Wang, R.X., Huang, Y.X., and Wang, Y.Z., 2021, Genesis of end-Guadalupian bauxite and pyrite deposits in the Youjiang Basin (South China): Insights into the causative link between magmatic events and mass extinction: Journal of Asian Earth Sciences, v. 215, https://doi.org/10.1016/j.jseaes.2021.104801.

Yin, R., Feng, X., Hurley, J.P., Krabbenhoft, D.P., Lepak, R.F., Hu, R., Zhang, Q., Li, Z., and Bi, X., 2016, Mercury isotopes as proxies to identify sources and environmental impacts of mercury in sphalerites: Scientific Reports, v. 6, https://doi.org/10.1038/srep18686.

Yu, W.C., Algeo, T.J., Du, Y.S., Zhang, Q.L., and Liang, Y.P., 2016, Mixed volcanogenic–lithogenic sources for Permian bauxite deposits in southwestern Youjiang Basin, South China, and their metallogenic significance: Sedimentary Geology, v. 341, p. 276–288, https://doi.org/10.1016/j.sedgeo.2016.04.016.

Yu, W.C., Algeo, T.J., Yan, J.X., Yang, J.H., Du, Y.S., Huang, X., and Weng, S.F., 2019, Climatic and hydrologic controls on upper Paleozoic bauxite deposits in South China: Earth-Science Reviews, v. 189, p. 159–176, https://doi.org/10.1016/j.earscirev.2018.06.014.

Zambardi, T., Sonke, J.E., Toutain, J.P., Sortino, F., and Shinohara, H., 2009, Mercury emissions and stable isotopic compositions at Vulcano Island (Italy): Earth and Planetary Science Letters, v. 277, p. 236–243, https://doi.org/10.1016/j.epsl.2008.10.023.

Zanoni, G., Segvic, B., and Moscariello, A., 2016, Clay mineral diagenesis in Cretaceous clastic reservoirs from West African passive margins (the South Gabon Basin) and its impact on regional geology and basin evolution history: Applied Clay Science, v. 134, p. 186–209, https://doi.org/10.1016/j.clay.2016.09.032.

Zarasvandi, A., Charchi, A., Carranza, E.J.M., and Alizadeh, B., 2008, Karst bauxite deposits in the Zagros Mountain Belt, Iran: Ore Geology Reviews, v. 34, p. 521–532, https://doi.org/10.1016/j.oregeorev.2008.05.005.

Zarasvandi, A., Carranza, E.J.M., and Ellahi, S.S., 2012, Geological, geochemical, and mineralogical characteristics of the Mandan and Deh-now bauxite deposits, Zagros Fold Belt, Iran: Ore Geology Reviews, v. 48, p. 125–138, https://doi.org/10.1016/j.oregeorev.2012.02.010.

Zhang, H., Yin, R.S., Feng, X.B., Sommar, J., Anderson, C.W.N., Sapkota, A., Fu, X.W., and Larssen, T., 2013, Atmospheric mercury inputs in montane soils increase with elevation: Evidence from mercury isotope signatures: Scientific Reports, v. 3, https://doi.org/10.1038/srep03322.

Zhang, Q.Z., 2011, Metallogenic model and exploration technology of bauxite in Western Guangxi, China [Ph.D. dissertation]: Beijing, China, China University of Geosciences, p. 1–150.

Zhang, S.H., Zhao, Y., Song, B., and Yang, Y.H., 2007, Zircon SHRIMP U-Pb and in situ Lu-Hf isotope analyses of a tuff from Western Beijing: Evidence for missing late Paleozoic volcano eruptions at the northern margin of the North China block: Gondwana Research, v. 12, p. 157–165, https://doi.org/10.1016/j.gr.2006.08.001.

Zhang, S.H., Zhao, Y., Song, B., Hu, J.M., Liu, S.W., Yang, Y.H., Chen, F.K., Liu, X.M., and Liu, J., 2009, Contrasting Late Carboniferous and Late Permian–Middle Triassic intrusive suites from the northern margin of the North China craton: Geochronology, petrogenesis and tectonic implications: Geological Society of America Bulletin, v. 121, p. 181–200.

Zhao, L.H., and Liu, X.F., 2019, Metallogenic and tectonic implications of detrital zircon U-Pb, Hf isotopes, and detrital rutile geochemistry of late carboniferous karstic bauxite on the southern margin of the North China Craton: Lithos, v. 350–351, https://doi.org/10.1016/j.lithos.2019.105222.

Zhao, L.H., Liu, X.F., Yang, S.J., Ma, X.L., Liu, L., and Sun, X.F., 2021, Regional multi-sources of Carboniferous karstic bauxite deposits in North China Craton: Insights from multi-proxy provenance systems: Sedimentary Geology, v. 421, https://doi.org/10.1016/j.sedgeo.2021.105958.

Zhou, M.F., Malpas, J., Song, X.Y., Robinson, P.T., Sun, M., Kennedy, A.K., Lesher, C.M., and Keays, R.R., 2002, A temporal link between the Emeishan large igneous province (SW China) and the end-Guadalupian mass extinction: Earth and Planetary Science Letters, v. 196, p. 113–122, https://doi.org/10.1016/S0012-821X(01)00608-2.

Zhou, X., Liu, D., Bu, H.L., Deng, L.L., Liu, H.M., Yuan, P., Du, P.X., and Song, H.Z., 2018, XRD-based quantitative analysis of clay minerals using reference intensity ratios, mineral intensity factors, Rietveld, and full pattern summation methods: A critical review: Solid Earth Sciences, v. 3, p. 16–29, https://doi.org/10.1016/j.sesci.2017.12.002.